Impact of ECCO Ocean State Estimates on the Initialization of Seasonal Climate Forecasts

Gabriel Cazes-Boezio* [1,3], Dimitris Menemenlis [2], and Carlos R. Mechoso [1]

1) Department of Atmospheric and Oceanic Sciences, University of California, Los Angeles

2) Jet Propulsion Laboratory, California Institute of Technology, Pasadena, California

3) Institute of Fluid Mechanics and Environmental Engineering (IMFIA), School of Engineering, University of Uruguay

[1] * Corresponding author adress:
Gabriel Cazes-Boezio, IMFIA, Facultad de Ingeniería, Julio Herrera y Reissig 565, Montevideo, Uruguay, 11300 (agcm@fing.edu.uy)

ABSTRACT

This article examines the impact of ocean state estimates generated by the consortium for Estimating the Circulation and Climate of the Ocean (ECCO) on the initialization of a Coupled General Circulation Model (CGCM) for seasonal climate forecasts. The CGCM consists of the University of California, Los Angeles Atmospheric GCM (UCLA AGCM) and of an ECCO ocean configuration of the Massachusetts Institute of Technology GCM (MITgcm). The forecasts correspond to ensemble seasonal hindcasts for the period 1993–2001. For the forecasts, the ocean component of the CGCM is initialized in either early March or in early June using ocean states provided either by an unconstrained forward ocean integration of the MITgcm (the "baseline" hindcasts) or by data-constrained ECCO results (the "ECCO" hindcasts). Forecast skill for both the baseline and the ECCO hindcasts is significantly higher than persistence and compares well with the skill of other state-of-the art CGCM forecast systems. For March initial conditions, the standard errors of Sea Surface Temperature (SST) anomalies in ECCO hindcasts (relative to observed anomalies) are up to 1º C smaller than in the baseline hindcasts over the central and eastern equatorial Pacific (150ºW-120ºW). For June initial conditions, the errors of ECCO hindcasts are up to 0.5º C smaller than in the baseline hindcasts. The smaller standard error of the ECCO hindcasts is, in part, due to a more realistic equatorial thermocline structure of the ECCO initial conditions. This study confirms the value of physically-consistent ocean state estimation for the initialization of seasonal climate forecasts.

1. Introduction

On time scales longer than one week, most of the memory of the coupled ocean-atmosphere system resides in the ocean. The successful prediction of the oceanic evolutions, therefore, is key for the success of long-range forecasts of El Niño-Southern Oscillation (ENSO) with Coupled atmosphere-ocean General Circulation Models (CGCMs) models (e.g., Rosati et al. 1997, Goddard et al. 2001). The initial oceanic conditions in these forecasts are usually obtained by application of a data assimilation system. For example, Behringer et al. (1998) describe a prediction system that assimilates temperature profiles from the Tropical Atmosphere Ocean (TAO) array using the approach of Derber and Rosati (1989). Ming et al. (2000) extend this methodology to include TOPEX/POSEIDON sea surface height data. Other examples of ocean data assimilation systems used to initialize ENSO predictions are given by Kirtman (2003), Wang et al. (2002), and Segschneider et al. (2001). The consensus is that the quality of oceanic initial conditions can have a significant impact on the success of ENSO predictions with CGCMs. For this, and for other reasons, several projects have been established with the objective of obtaining increasingly more accurate descriptions of the time evolving ocean circulation. One such effort is the consortium for Estimating the Circulation and Climate of the Ocean (ECCO). This paper evaluates the impact of ECCO initial conditions on the skill of seasonal climate forecasts by a CGCM.

The ECCO consortium was established in 1999 with support from the National Oceanographic Partnership Program (NOPP) in order to demonstrate the practicality and utility of state estimation for global-scale physical oceanography. The principal partners of the ECCO project (1999-2005) were the Massachusetts Institute of Technology (MIT), the Scripps Institution of Oceanography (SIO), and NASA's Jet Propulsion Laboratory

(JPL). A distinguishing feature of ECCO ocean state estimates is their physical consistency. Estimates are obtained by least-squares fit of the MIT general circulation model (MITgcm) to the available observations; the estimates satisfy the model's time-evolution equations, budgets of fluid properties are balanced, there are no discontinuities when new data are inserted, and error covariance is propagated through the same physical model as the state vector, hence more fully utilizing the available data. The demonstration solutions obtained by ECCO still have several shortcomings, which are being addressed as part of ECCO-follow-on projects. Nevertheless, these demonstration solutions have proved scientifically useful for a large number of oceanographic and interdisciplinary studies on topics such as the ocean general circulation (e.g., Stammer et al. 2003; Gebbie et al. 2004), biogeochemical cycles (e.g., McKinley et al. 2003), air-sea fluxes (e.g., Stammer et al. 2004), subgrid scale parameterizations (e.g., Ferreira et al. 2005), and geodetic studies (e.g., Gross et al. 2004).

Dommenget and Stammer (2004) used ECCO ocean state estimates to initialize seasonal climate hindcasts and reported that initial ocean conditions and forcing corrections calculated by ocean-state estimation have a positive impact on ENSO predictive skill. Hindcast skills in that study, however, are limited by the use of a statistical atmosphere and by the coarse horizontal resolution of the ocean model, which has 2º horizontal grid spacing. In the present study we obtain short-term climate hindcasts using a CGCM that comprises the University of California, Los Angeles Atmospheric GCM (UCLA AGCM) coupled to a quasi-global ocean configuration of the MITgcm that has 1/3-degree meridional grid spacing at the Equator. In a separate study, experimental climate forecasts are also being attempted using the same MITgcm configuration, coupled to the National Centers for Environmental Prediction (NCEP) Atmospheric Global Spectral

Model (Yulaeva, Kanamitsu, and Roads, 2007). Here, our specific objective is to compare seasonal ENSO hindcasts in which the ocean component is initialized using states from (i) an unconstrained baseline simulation of the MITgcm and (ii) a data-constrained solution provided by the ECCO project.

The remainder of this article is organized as follows. Section 2 describes the baseline MITgcm integration and the constrained ECCO solution that are used to initialize CGCM hindcasts. Section 3 describes the selected UCLA AGCM configuration and presents results from a 41-year-long integration of this AGCM coupled to an ECCO ocean configuration of the MITgcm. Section 4 discusses results from experimental forecasts obtained using the above CGCM during the 1993–2001 period. Section 5 compares these results to hindcasts from other state-of-the-art CGCM ENSO prediction systems. Summary and concluding remarks follow in Section 6.

2. Baseline and optimized ECCO solutions

The ECCO solution used in the Dommenget and Stammer (2004) study was computed using a quasi-global (80°S to 80°N) configuration of the MITgcm (Marshall et al., 1997) with 2° horizontal grid spacing, both in latitude and in longitude, and with 23 vertical levels. To better resolve equatorial processes the present study uses an ECCO/MITgcm configuration and solution with enhanced horizontal and vertical resolutions. The ocean model configuration is the one used for a quasi-operational analysis, which is maintained at JPL. The analysis is updated approximately once per week, it is freely available (http://ecco.jpl.nasa.gov), and it is being used for a variety of science applications (e.g., Lee et al. 2002; Dickey et al. 2002; Lee and Fukumori 2003; McKinley et al. 2003; Gross

et al. 2003, 2004; Fukumori et al. 2004; Wang et al. 2004a, b; Kim et al. 2004). The specific ECCO/JPL ocean model configuration and the particular baseline and optimized ECCO solutions used in this study are described next.

a. Baseline MITgcm integration

The ECCO/JPL near-real-time analysis is based on a quasi-global (73°S to 73°N) configuration of the MITgcm with a horizontal grid that has 360 and 224 zonal and meridional grid cells, respectively. Zonal grid spacing is 1° of longitude. Meridional grid spacing is 0.3° of latitude within 10° of the Equator and increases to 1° latitude poleward of 22°N and of 22°S. The model configuration has 46 vertical levels; the levels are 10-m-thick in the top 150 m; below that, level thicknesses gradually increase to a maximum of 400 m near the bottom; the maximum model depth is 5815 m. The bathymetry is based on ETOPO5 (Data Announcement 88MGG-02, Digital relief of the Surface of the Earth, NOAA, National Geophysical Data Center, Boulder, Colorado, 1988). The model employs the K-Profile Parameterization (KPP) vertical mixing scheme of Large et al. (1994) and the isopycnal mixing schemes of Redi (1982) and of Gent and McWilliams (1990) with surface tapering as per Large et al. (1997). Laplacian diffusion and friction are used, except that horizontal friction is biharmonic. Lateral boundary conditions are closed. No-slip bottom, free-slip lateral, and free surface boundary conditions are employed. Surface freshwater fluxes are applied as virtual salt fluxes. Isopycnal diffusivity and isopycnal thickness diffusivity is 500 $m^2\ s^{-1}$. Vertical diffusivity is 5×10^{-6} $m^2\ s^{-1}$. Horizontal and vertical viscosities are 10^{13} $m^4\ s^{-1}$ and 10^{-4} m2 s^{-1}, respectively.

The baseline integration was carried out in two steps by the ECCO/JPL group. In a first step the model was integrated for ten years from zero initial velocities and from initial temperature and salinity conditions obtained from the National Oceanographic Data

Center (NODC) World Ocean Atlas 1998 (WOA98); surface forcing was from a mean seasonal cycle computed for the period 1980-1997 from the NCEP meteorological reanalysis (Kistler et al. 2001). In a second step the model was integrated from January 1980 to present starting from initial conditions corresponding to the end of Step 1 and forced at the surface with 12-hourly wind stress and daily heat and freshwater fluxes, which were obtained from the NCEP meteorological reanalysis with following modifications: (i) the 1980 to 1997 time-mean fluxes were subtracted and replaced with the 1945 to 1993, time-mean, Comprehensive Ocean-Atmosphere Data Set (COADS) fluxes (Woodruff et al. 1998); (ii) the 1945 to 1993 time-mean COADS heat and freshwater fluxes were further adjusted so that they have zero mean over the model domain; (iii) Sea Surface Temperature (SST) was relaxed to NCEP SST using the formulation of Barnier et al. (1995); (iv) shortwave is depth-penetrating using the formula of Paulson and Simpson (1977); (v) any model temperature that becomes less than -1.8°C is reset to -1.8°C in order to simulate the freezing of sea-water; and (vi) Sea Surface Salinity (SSS) is relaxed to monthly mean SSS from WOA98 with a relaxation constant of 60 days. A formal justification of above choices is beyond the scope of present manuscript. Suffice to say that they were the result of dozens of trial-and-error experiments over the course of several years by a handful of experienced physical oceanographers. Furthermore, all of the above choices were later adjusted using data constraints, as is described next.

b. Data-constrained ECCO solution

We use in this study the so-called smoothed wind-driven ECCO/JPL solution (available at http://ecco.jpl.nasa.gov/cgi-bin/nph-dods/datasets/dr049f/). The data used to constrain the baseline integration are observations of sea surface height and a collection of vertical

temperature profiles. Sea surface height data are from the National Aeronautics and Space Administration Goddard Space Flight Center (NASA GSFC) Pathfinder Topographic Ocean Experiment (TOPEX)/Poseidon Altimetry Version 9.1 (http://podaac.jpl.nasa.gov). Specifically, colinear sea surface height data are used, which are georeferenced to a specific ground track and are given at 1-s intervals, approximately every 6 km along each track. The data are corrected for all known geophysical, media, and instrument effects, including tides and atmospheric loading. The Pathfinder information is further bin-averaged along each track, consistent with the model resolution. Vertical temperature profile data from expendable bathythermographs (XBTs), from the Tropical Atmosphere Ocean (TAO) array, and from the Argo global array of free-drifting profiling floats are processed, quality checked, and made available by D. Behringer (2002, personal communication). These data are complemented with temperature profiles from the World Ocean Circulation Experiment (WOCE), from the Hawaii Ocean Time Series (HOTS), from the Bermuda Atlantic Time Series (BATS), and from Profiling Autonomous Lagrangian Circulation Explorer (PALACE) floats. The temperature data are bin-averaged inside each model grid box and for 10-day intervals.

The constrained ECCO/JPL analysis is obtained in two steps. In a first step, the Green's function approach of Menemenlis et al. (2005) is used to calibrate the model's internal mixing parameters, the initial temperature and salinity conditions, the SST and SSS relaxation coefficients, and the time-mean surface wind stress. Of particular importance for the Equatorial thermocline structure is the vertical diffusivity parameter, which is increased from 5×10^{-6} m^2 s^{-1} to 15×10^{-6} m^2 s^{-1}. In a second step, the approximate Kalman filter and the smoother of Fukumori (2002) are used to correct residual adiabatic time-dependent errors. A detailed comparison of the baseline and data-constrained solutions is

in Menemenlis et al. (2005). In reference to observations, the data-constrained solution has significantly less bias and drift and explains 10% to 30% more variance than the baseline integration. The bias reduction of the constrained ECCO/JPL solution is most significant at the base of the equatorial thermocline (compare Figs. 13c and 13e in Menemenlis et al. 2005). To a large extent this is the result of vertical diffusivity being too weak in the baseline integration, hence resulting in a thermocline that is too sharp and too shallow relative to data. Section 4 further discusses and analyzes these differences and their consequences.

3. Description of the UCLA/MIT CGCM

The CGCM used in this study comprises the optimized MITgcm ocean model configuration described above, which is coupled to the UCLA AGCM described next.

a. UCLA AGCM

The UCLA AGCM is a finite difference model that integrates the primitive equations of the atmosphere. The model's horizontal and vertical discretizations are arranged as "C" and Lorenz grids, respectively. The parameterizations of the major physical processes include solar and terrestrial radiation calculations according to Harshvandan et al. (1987 and 1989, respectively), and the cumulus convection scheme of Arakawa and Schubert (1974) as revised by Pan and Randall (1994). The UCLA AGCM configuration used in this study has 15 vertical layers and has horizontal grid spacing of 5^o in longitude and 4^o degrees in latitude.

The quality of simulated surface fluxes of momentum, of latent and sensible heat, and of water vapor mass exchanged between the atmosphere and the underlying surface are of

crucial importance for the success of CGCM simulations. Those fluxes are provided by the parameterization of the Planetary Boundary Layer (PBL) processes of the AGCM; this parameterization also provides PBL cloudiness. PBL clouds strongly influence surface radiation fluxes and hence the predicted SSTs (Ma et al. 1996, Mechoso et al. 2000). The AGCM version used in this paper has a revised PBL parameterization (Konor and Arakawa 2005), in which Turbulent Kinetic Energy (TKE) vertically averaged through the PBL is a prognostic variable, which is used for the computation of surface fluxes of moisture, sensible heat, and momentum. TKE is also used for an explicit formulation of the mass entrainment rate at the top of the PBL following Randall and Schubert (2004). The new parameterization allows for several layers within the PBL and hence for vertical wind shears and for departures of thermodynamic variables from well-mixed vertical profiles. In the present paper we use an intermediate stage of development of this parameterization that uses the new formulation of surface fluxes and mass entrainment rate at the top of the PBL but that considers the PBL to be well mixed.

b. Results from a multi-decadal integration of the UCLA/MIT CGCM

The MITgcm ocean model and the UCLA AGCM have been coupled using both the UCLA Earth System Model (ESM) and the Earth System Modeling Framework (ESMF) couplers. The MITgcm is configured as described in Section 2 and it is coupled to the version of the UCLA AGCM described above without any flux correction. In this section we evaluate the performance of this CGCM through analysis of selected results from a 41-year-long integration, which is initialized from conditions corresponding to January 10 of long, uncoupled simulations of the two component models.

Figures 1a and 1b show, respectively, simulated and observed annual mean SST. The verification data set is a 1971–2000 climatology from the NOAA Extended

Reconstructed SST, as provided by the NOAA-CIRES ESRL/PSD Climate Diagnostics Branch, Boulder, Colorado, USA (http://www.cdc.noaa.gov). Figure 1c shows the difference between simulated and observed fields. The simulated zonal SST gradient in the equatorial Pacific is approximately 4ºC, which compares well to the observed SST gradient of approximately 5ºC. The simulation reproduces the cold tongue in the tropical eastern Pacific and realistically captures its asymmetry with respect to the equator. In the Equatorial Atlantic, the zonal SST gradient has the correct sign; this is a particularly difficult task for non-flux corrected models (De Witt 2005; Davey et al. 2002). The simulated magnitude of the gradient, however, is approximately half of the observed gradient. In the Tropical Southern Pacific and Atlantic Oceans, the simulated warm pool extends too far to the east, as is also the case for precipitation (not shown). The model, therefore, shares with others the simulation of a spurious double Intertropical Convergence Zone (ITCZ) (Mechoso et al. 1995). The simulated SST in the Eastern Equatorial Pacific is approximately 1ºC colder than the observations. Model errors along the eastern coasts of the tropical oceans, however, are small.

To assess the capability of this coupled model to simulate the interannual variability of the Equatorial Pacific, Hovmöller diagrams of monthly mean SST and zonal wind stress anomalies averaged between 4ºS and 4ºN are shown in Figs. 2a and 2b, respectively. The Fig.-2 anomalies exhibit ENSO-like characteristics, with weaker and stronger trade winds associated with warm and cold SST anomalies, respectively. As in the observations, the strongest SST anomalies usually appear in the Eastern Pacific during the boreal winter. The simulated ENSO-like signal in the 41-year simulation has a period between 3 and 7 years and amplitude of 1ºC to 2ºC. The location of strongest wind stress anomalies tends to be shifted westward with respect to the strongest SST anomalies, as is typically

observed during ENSO episodes. Correlations between simulated SST in the Niño 3.4 region (120ºW-170ºW, 5ºS-5ºN) and Sea Level Pressure (SLP) provide a quantitative evaluation of the CGCM's ability to reproduce observed associations between oceanic and atmospheric anomalies. Figure 3 shows such correlations for the November–December period, when ENSO tends to peak, for the simulation (Fig. 3a) and for observed Niño 3.4 SST versus NCEP reanalysis SLP (Fig. 3b). The simulated Southern Oscillation pattern (Fig. 3a) is comparable with that computed from observation (Fig. 3b).

AchutaRao and Sperber (2002) describe the simulation of ENSO by 17 global CGCMs from the Coupled Model Intercomparison Project (CMIP). The simulations are 80-year long and about half of the models do not apply flux correction algorithms. Flux-corrected models produced a better simulation of the annual cycle of the temperature field in the Equatorial Pacific but not necessarily a better simulation of ENSO variability. A few of the CMIP models simulate the SST variability in the equatorial eastern Pacific with realistic amplitude but in many CMIP models ENSO tends to occur at a higher frequency than in the observation. While a few of the CMIP models have Walker cell anomalies associated with ENSO that compare well with the observations, many of the CMIP models have Walker cell anomalies that are shifted to the west or are too weak. The interannual variability of the CGCM simulation used in this study shares positive aspects with some of the more realistic CMIP models, for example, irregular ENSO-like variability and realistic geographical patterns of Walker cell anomalies associated with ENSO. Earlier versions of the UCLA AGCM coupled with a regional Pacific configuration of the Geophysical Fluid Dynamics Laboratory (GFDL) ocean model also showed ENSO-like variability with realistic features (Yu and Mechoso 2001, Mechoso et

al. 2000). The CGCM version used here, however, has smaller errors in surface heat fluxes (not shown) and a less pronounced double ITCZ.

Wang et al. (2005) introduced a new version of the NCEP coupled forecast system model, in which the operational version of the NCEP global forecast system model is configured at a relatively high resolution (T62 in the horizontal and 64 layers in the vertical) and is coupled with the Modular Ocean Model (MOM) version 3 without flux corrections. A 32-year simulation of this CGCM shows ENSO variability with realistic features, which indicates that the model is suitable for real-time ENSO prediction. The UCLA CGCM simulation presented here has a larger negative SST bias at the Equator and a larger double ITCZ bias than the results presented by Wang et al. (2005). Nevertheless, it has a smaller SST bias in the stratocumulus region of the Southeastern Tropical Pacific despite the coarser resolution.

4. Experimental forecasts

In this section we discuss various hindcasts obtained by the UCLA/MIT CGCM just described. We produced four sets of 15-month-long ensemble hindcasts during the 1993 to 2001 period. Two sets of hindcasts were initialized on, respectively, March-5 and June-5 of each year using oceanic conditions obtained from the baseline MITgcm simulation described in Section 2a. Hereinafter we refer to these ensemble-hindcasts as "baseline hindcasts". Two more sets of hindcasts were initialized on March 5 and on June 5 of each year using oceanic conditions from the ECCO solution described in Section 2b. Hereinafter we refer to these ensemble-hindcasts as "ECCO hindcasts". For each different set of oceanic initial condition, 5 ensemble members were computed, each

initialized with slightly different atmospheric initial conditions. The atmospheric initial conditions are taken from a long uncoupled simulation with climatological SSTs. The choice of early-March and early-June initial conditions allows comparing hindcasts before and after the spring predictability barrier, which occurs around April.

Next we discuss some aspects of the simulated mean temperature fields in the Pacific Ocean for each of the hindcast sets. Figure 4 shows vertical temperature sections averaged between 2ºS and 2ºN in the Pacific Ocean for the mean 1993–2001 initial conditions of each set. The baseline initial conditions for March 5 (Fig. 4b) have a thermocline that is sharper, shallower, and less realistic than the equivalent ECCO initial conditions, in agreement with the results of Menemenlis et al. (2005). Baseline initial conditions for June 5 also show a sharper thermocline than the equivalent ECCO initial conditions, although less so than for March.

Departures of these mean initial conditions with respect to the UCLA/MIT CGCM climatology produce a short-term mean bias that can span part or all of the hindcast duration. Figure 5 shows the difference between the mean initial conditions shown on Fig. 4 and the corresponding March or June CGCM climatology. The CGCM climatology is defined as the average over the 41-year CGCM simulation period described in Section 3. For all the sets of initial conditions we find a cold bias with respect to CGCM climatology in the thermocline region, which corresponds to a deeper thermocline in the CGCM climatology than in the initial conditions. This bias in the initial conditions leads to a cold SST bias with respect to the CGCM climatology in the eastern and central Equatorial Pacific for the December–February (DJF) hindcast period (Fig. 6). Hereinafter, in order to reduce the impact of CGCM drift in response to initialization

bias, we examine anomalies obtained by subtracting from the hindcast results of each set the 1993–2001 ensemble mean of all hindcast members in that set.

Figures 7a and 7b show the skill in the prediction of mean SST for the DJF period of ECCO and baseline hindcasts initialized during the preceding March 5. Figure 7c shows skill of the persistence forecast, which is defined as the March SST anomaly. Skill is here defined as the correlation of predicted versus observed SST anomalies in the 1993 to 2001 hindcasting period. Contours above 0.6 and below −0.6 are displayed, which correspond to values with a 95% statistical significance level according to the Student-t test for 9 degrees of freedom. The skill of both ECCO and baseline hindcasts in the equatorial region is rather high, with values around 0.8. The corresponding skill of persistence hindcasts is much lower. Figures 7d-f are similar to Figs. 7a-c, except that hindcasts are initialized on June-5 and the persistence hindcast is defined as the June SST anomaly. Here again, the skill of both ECCO and baseline hindcasts are quite high, with values around 0.90. The skill of persistence hindcasts initialized in June (Fig. 7f) is much higher than that of persistence hindcasts initialized in March (Fig. 7c) due to the spring predictability barrier.

Figures 8a, b, and c show the standard error of ECCO, baseline, and persistence hindcasts initialized on March-5 for predicting DJF SST. Standard error is defined as the root-mean-square difference between predicted and observed SST anomaly. Figure 9a shows the difference of Fig. 8b minus Fig. 8a, that is, the amount of standard error reduction when the hindcasts are initialized with ECCO rather than with baseline initial conditions for March-5. Shaded areas correspond to values that are statistically significant at the 95% confidence level. Statistical significance in this case was estimated through a Monte-Carlo two-side test, in which differences of standard error between 1000 random

combinations of sets of 9 ECCO and baseline hindcasts are considered. Figures 8d, e, and f, and Fig. 9b show the corresponding results for hindcasts initialized on June. For hindcasts initiated in March, the standard errors are 0.25ºC to 1ºC larger for the baseline hindcasts than for the ECCO hindcasts in the central to eastern Equatorial Pacific. Persistence hindcasts show even larger errors, with values as high as 2ºC over most of the Equatorial Pacific (Fig. 8c). For the hindcasts initialized in June, the comparison between standard errors for ECCO, baseline, and persistence predictions give qualitatively similar results but the differences have smaller magnitude than for the hindcasts initialized in March.

Figure 10 shows the evolution in time of hindcast skill for the Niño 3.4 region for CGCM integrations initialized on March-5 (upper panel) and on June (lower panel). The skill of both ECCO and baseline hindcasts remains high for almost a full year. The skill of persistence hindcasts initialized in March decreases to very low values after May of the same year while the skill of persistence hindcasts initialized in June remains high (around 0.9) until April of the following year. Figures 11a and 11b show Niño-3.4 standard error for CGCM integrations initialized on, respectively, March 5 and June 5. As was the case for skill and standard error maps for DJF in Figs. 7 and 8, the standard error in the Niño 3.4 region (Fig. 11) is substantially less for the ECCO than for the baseline hindcasts although Niño 3.4 skills are similar (Fig. 10). The standard error of the baseline hindcasts initialized in March is larger than that of the ECCO hindcasts by up to 0.5ºC, while the standard error of the baseline hindcasts initialized in June is larger than that of the ECCO hindcasts by up to 0.25ºC.

To check whether the increased standard error of the baseline hindcasts is due to increased intra-ensemble forecast spread, Fig. 12 shows the intra-ensemble standard

deviation of DJF SST for each hindcast set. Standard deviation is computed for the five ensemble members in each year and then averaged through the 1993–2001 period. Intra-ensemble dispersion is similar for the ECCO and for the baseline hindcasts that are initialized in March; the ECCO hindcasts initialized in June have slightly smaller dispersion than the corresponding baseline hindcasts. Additionally the forecast spread of the baseline hindcasts (Figs. 12b and d) is approximately half the standard error of the baseline hindcasts (Figs. 8b and e). In summary, the ECCO and the baseline hindcasts have comparable skill in the prediction of SST anomalies and similar intra ensemble dispersion but differ significantly in terms of standard errors, especially for the hindcasts initialized on March-5. Therefore intra-ensemble variability does not fully account for the increased standard error of the baseline hindcasts relative to the ECCO hindcasts.

The ECCO and the baseline hindcasts differ only in the oceanic initial conditions. To gain insight on the structure of these initial differences, we examine the interannual standard deviation of the March-5 ECCO and baseline initial conditions in the Equatorial Pacific. Figures 13a and 13b show the standard deviation of the interannual anomalies for the March-5 ECCO and baseline initial conditions. We conjecture that since the anomalous vertical displacement of regions of high vertical gradient results in large temperature anomalies, the standard deviation of the baseline initial conditions is larger than that of the ECCO initial conditions because the baseline initial conditions have a sharper mean thermocline (cf. Fig. 4a and 4b). This difference is up to 1ºC at the base of the thermocline in the central-to-eastern Equatorial Pacific (Fig. 13c). Figure 14 shows vertical sections of baseline temperature standard deviation minus ECCO temperature standard deviation in the Equatorial Pacific Ocean for hindcasts initialized on March 5 for the periods March-to-May (Fig 14a), June-to-August (Fig. 14b), September-to-November

(Fig. 14c) and December-to-February (Fig. 14d). As for the initial conditions, the baseline hindcasts have larger interannual anomalies than the ECCO hindcasts. Based on this evidence, we hypothesize that the unrealistically sharp and shallow equatorial thermocline in the baseline initial conditions leads to hindcasts that have unrealistically large SST variability among realizations. For example, the standard deviation of DJF Niño 3.4 SST from 1993 to 2001 is 1.30ºC for observations, which is comparable to 1.26ºC for ECCO hindcasts initialized in March. By way of contrast, the standard deviation of DJF Niño 3.4 SST from 1993 to 2001 is 1.79ºC for baseline hindcasts initialized in March. Note that the larger interannual standard deviation for the baseline hindcasts set does not necessarily reflect on the intra-ensemble standard deviation, as shown in Fig. 12. This is because the interannual standard deviation of the hindcast simulations is associated with the interannual variability of the initial conditions sets, while intra-ensemble standard deviation is linked with the CGCM's sensitivity to perturbations in the initial conditions.

In order to complete the assessment of the forecast system performance, we also carry out a preliminary evaluation of the skill of probability hindcasts. Since sample size is rather limited, we define two categories — (i) SST above and (ii) SST below the median — and focus on the Niño-3.4 index during the DJF period. We compute the DJF median of this index using all integrations in each hindcast set and we estimate the probability of the Niño-3.4 index to be above the median in any given year as the proportion of ensemble members, out of the five ensemble members in each year, above the median of the entire set. Brier skill scores (Wilks 1995) of these predictions are shown in Table 1. The reference score refers to a climatological hindcast of probability 0.5, which correspond to a Brier skill score of 0.25. Brier skill scores for hindcasts initialized in June are

statistically significant above the 95% level, both for the ECCO as well as for the baseline hindcasts. Here, statistical significance is estimated by using a Monte-Carlo test of 1000 realizations. In each realization probability hindcasts are issued for each year from 1993 to 2001 by taking five random binary choices. Brier skill score for ECCO hindcasts initialized in March is also significant above the 95% level. Brier skill score for baseline hindcasts initialized in March, however, is not significant at the 95% level. An important contribution to the poorer performance of the baseline hindcasts initialized in March is the failure of the hindcasts during two years with small anomalies, 1996 and 2001. Although categorical forecasts for a larger number of categories may be of help in such situations, this would require larger hindcast ensembles than were available for this study.

5. Comparison to other CGCM ENSO prediction systems

In this section we compare the ECCO and the baseline hindcasts just described to some state-of-the-art CGCM SST forecast systems, in which the atmospheric and oceanic GCMs are coupled without flux corrections. Palmer et al. (2004) describe the Development of a European Multimodel Ensemble system for seasonal to inTERannual prediction (DEMETER). Ensemble predictions from several coupled models are combined into a multi ensemble forecast. Ensemble hindcast results from individual model components of DEMETER are also made available. For comparison purposes we use results from one of these models, the European Centre for Medium Range Weather Forecasts (ECMWF) coupled ocean-atmosphere forecast system. A description of this coupled model is in Segschneider et al. (2001). DEMETER hindcasts are initialized in February, May, August, and November.

De Witt et al. (2004a, b) use both the ECMWF-Hamburg (ECHAM) model version 4.5 and the Center for Ocean–Land–Atmosphere (COLA) version 2 AGCMs, coupled with the MOM version 3 OGCM, hereinafter referred to as the ECHAM/MOM and the COLA/MOM CGCMs. The ocean initial conditions are taken from the ocean data assimilation system of Derber and Rosati (1989), which is maintained at the Geophysical Fluid Dynamics Laboratory (GFDL). Hindcasts are initialized in April (De Witt et al. 2004a) and in July (De Witt et al. 2004b) for the years 1982 to 2003.

Saha et al. (2006) present results from the Climate Forecast System (CFS), which is operational at NCEP. The CFS consists of the NCEP Global Forecast System (GFS) atmospheric model (Moorthi et al. 2001) with a spectral T62 truncation and with 64 levels in the vertical, coupled with the MOM version 3 OGCM. The ocean initial conditions are provided by the Global Ocean Data Assimilation System (GODAS) described in Behringer et al. (2005). Hindcasts are initialized during each month from 1982 to 2003 and the results are publicly available. For comparison purposes, we only consider hindcasts initialized in March and in June.

Table 2 shows the skill and standard error for 6-months-lead hindcasts of the Niño-3.4 SST anomaly index for the hindcasts produced by the systems described in the previous paragraphs (ECMWF, ECHAM/MOM, ECHAM/COLA, and NCEP CFS) and for the ECCO and baseline hindcasts presented in section 4 of this work. Figure 15 summarizes the time lead evolution of hindcast skill and of standard error for the subset of above forecast systems for which hindcast data is readily available. Overall, ECCO hindcasts initialized in March perform slightly better than ECMWF hindcasts initialized in February while the NCEP CFS hindcasts initialized in June and the ECMWF hindcasts initialized in May perform slightly better than the ECCO hindcasts initialized in June.

Table 1 and Fig. 5 show that despite the small number of hindcast elements and despite the coarse resolution of the UCLA AGCM configuration, which were used in this preliminary study, the ECCO hindcasts can be of comparable or better quality than hindcasts from state-of-the-art forecast systems.

6. Summary, discussion, and concluding remarks

This study evaluated the impact of ocean state estimates generated by the ECCO project on the initialization of a CGCM for seasonal climate forecasts of ENSO. Hindcasts were obtained with a CGCM consisting of the UCLA AGCM coupled without flux corrections to the MITgcm ocean model. In a 41-year simulation, this UCLA/MIT CGCM demonstrates an ability to realistically capture key features of the tropical climate. For example, the strength of the equatorial SST gradient in the Pacific Ocean is comparable with observations. Also, the cold tongue in the eastern Equatorial Pacific has a strong asymmetry with respect to the Equator, as observed. The simulation produces interannual SST anomalies in the equatorial Pacific that resemble ENSO, including the known association between wind stress and SLP anomalies.

Forecast skill for this CGCM was evaluated using a series of ensemble-hindcast experiments. Hindcasts in each ensemble are initialized either in early March or in early June for the years 1993–2001 and integrated for 15 months. The oceanic initial conditions are provided by the ECCO analysis and by a baseline simulation of the uncoupled MITgcm ocean model. The atmospheric initial conditions are taken from a long uncoupled simulation with climatological SSTs. Both the ECCO and the baseline hindcasts initialized in either March or in June have high skill. For the Niño 3.4 SST anomaly index, this is approximately 0.8 and 0.9 for March and for June initial conditions, respectively, for time leads up to 9 months (Fig. 10). Standard error for SST

anomaly in the DJF period for hindcasts initialized in March is approximately 0.7ºC and 1.1ºC for, respectively, ECCO and baseline initial conditions (Figs. 11a). For hindcasts initialized in June, standard SST anomaly error is approximately 0.5ºC and 0.6ºC for, respectively, ECCO and baseline initial conditions (Figs. 11b).

SST anomaly persistence hindcasts initialized in June show a skill for the whole Niño 3.4 region comparable to that obtained with the ECCO and with the baseline hindcasts (Fig. 10b). SST persistence hindcasts initialized in March, however, show negligible skill for time leads larger than two months, unlike the corresponding ECCO and baseline hindcasts, which continue to have relatively high skill (>0.8) until the following June (Fig. 10a). This suggests that during March, both the ECCO and the baseline oceanic initial conditions contain subsurface information that is relevant for predictability. To explore this hypothesis, we compute the correlation of Niño 3.4 SST anomalies in the DJF period with respect to both the ECCO and the baseline oceanic initial conditions. Figures 16a and 16c show correlation of DJF Niño 3.4 index with oceanic temperature averaged between 2ºS and 2ºN for, respectively, the March-5 and the June-5 ECCO initial conditions. Figures 16b and 16d show the same quantities for the baseline initial conditions. For the March-5 ECCO and baseline initial conditions (Figs. 16a and 16b) there is statistically significant correlation mostly around the respective climatological thermoclines but not at the sea surface.

Since the thermocline is a region of large vertical temperature gradients, temperature anomalies in this region are to first order associated with vertical displacements, which in turn are primarily driven by changes in surface wind stress. For this reason, both the baseline integration, which is driven by NCEP reanalysis surface wind stress, and the ECCO solution contain subsurface information in March that is correlated with Niño 3.4

SST several months later. This also explains the success of both baseline and ECCO hindcasts in terms of skill. Hindcasts initialized from March baseline initial conditions, however, have significantly higher standard error than the corresponding ECCO hindcasts (Fig. 9a and 11a). We hypothesize that the higher success of the ECCO hindcasts is due to differences in the information provided at the ocean subsurface, specifically, because of the more realistic equatorial thermocline of the ECCO solution relative to that of the baseline integration. That is, the sharper and shallower thermocline of the baseline integration relative to ECCO and relative to observations causes larger SST anomalies in the resulting hindcasts.

Unlike the March-5 initial conditions, the cases with June-5 initial conditions are significantly correlated with DJF Niño 3.4 index at the sea surface (Figs. 16c and 16d), suggesting that information relevant to DJF predictability has typically outcropped to the sea surface by June. Nevertheless, hindcasts initialized from baseline June-5 initial conditions have SST standard errors that are larger than hindcasts initialized from ECCO June-5 initial conditions (Figs. 9b and 11b).

One limitation of this study is the small size of the record (1993 to 2001), which is used to test the ECCO hindcasts. In particular, the strong 1997-1998 ENSO episode could make the results appear more statistically significant than they really are. Nevertheless, if the 1997-1998 episode is excluded, skill of all the hindcast sets drop but remain at levels that are both relatively high and statistically significant (above 95% level), while standard error remain practically the same. In particular, standard error for the baseline hindcast sets is still higher than for the respective ECCO sets. Table 3 summarizes hindcast skill and standard error for DJF Niño 3.4 SST anomaly index for each hindcast set, considering the whole 1993-2001 period and excluding the 1997-1998 case.

The results of this study confirm the importance of oceanic initial conditions for seasonal ENSO forecasts, as was already found in many of the studies referenced herein. The ready availability of ESMF coupling technology and of initial conditions generated by the ECCO project made it possible for a relatively modest effort to construct a CGCM ENSO forecasting system that has skill approaching and in some cases surpassing that of state-of-the-art CGCM ENSO prediction systems. The results of this study can be improved in many ways; for example, through the use of higher resolution and of more realistic UCLA AGCM and MITgcm configurations, through the use of more up-to-date ECCO initial conditions, through the use of a larger number of members in each ensemble hindcast, and through the use of estimation techniques to better calibrate the UCLA/MIT CGCM in order to reduce CGCM biases. Despite many limitations, the results of this study demonstrate the value of physically consistent ocean state estimation for initializing seasonal ENSO forecasts.

Acknowledgements: This research was supported by NASA CAN 2145/041 and NOAA Grant NA030AR4310095. Dr. Celal Konor directed the implementation of the upgraded PBL parameterization in the UCLA AGCM. CGCM integrations were carried using supercomputers made available by the NASA Ames Research Center and by the Jet Propulsion Laboratory. Hindcast results from the ECMWF coupled model forecast system were made available by the DEMETER project. NCEP's CFS results were made available by NCEP.

References

AchutaRao K. and K. R. Sperber, 2002: Simulation of the El Ninio Southern Oscillation: Results form the Coupled Model Intercomparison Project. *Climate Dyn*., **19** 191-209.

Arakawa, A., and W. H. Schubert, 1974: Interaction of a cumulus cloud ensemble with the large-scale environment, Part I. *J. Atmos. Sci.*, **31**, 674-701.

Barnier, B., L. Siefridt, and P. Marchesiello, 1995: Thermal forcing for a global ocean circulation model using a three-year climatology of ECMWF analysis. *J. Mar. Sys.*, **6**, 363–380.

Behringer D. W., M. Ji and A. Leetmaa, 1998: An improved coupled model for ENSO prediction and implications for ocean initialization. Part I: The ocean data assimilation system. *Mon. Wea. Rev.,* **126**, 1013-1021.

Behringer, D. W., et al., 2005, The Global Ocean Data Assimilation System (GODAS) at NCEP, to be submitted for publication

Davey M. K. [list of coauthors], 2002: STOIC: a study of coupled model climatology and variability in tropical ocean regions. *Climate Dyn*., **18** 403-420.

Dickey, J. O., S. L. Marcus, O. de Viron, and I. Fukumori, 2002: Recent Earth oblateness variations: Unraveling climate and postglacial rebound effects. *Science*, **298**, 1975–1977.

Dommenget, D., and D. Stammer, 2004: Assessing ENSO simulations and predictions using adjoint ocean state estimation. *J. Clim.*, **17**(22), 4301–4315.

Derber J. D. and A. Rosati, 1989: A global oceanic data assimilation system. *J. Phys. Oceanogr,* **19**, 1333-1347.

De Witt D. G., 2005: Diagnosis of the tropical Atlantic near-equatorial SST bias in a directly coupled atmosphere-ocean general circulation model. *Geophys. Res. Let.*, **32**, L01703.

De Witt D. G., E. K. Schneider and Z. Z. Hu, 2004 (a): Tropical Pacific SST forecasts utilizing multiple coupled GCMs, *Experimental Long lead Forecasts* Bulletin, **13**, Nº 2, Center for Ocean-Land-Atmosphere Studies, xx pp [available at http://www.iges.org/ellfb].

De Witt S. G., E. K. Schneider and Z. Z. Hu, 2004 (b): Tropical Pacific SST forecasts utilizing multiple coupled GCMs, *Experimental Long lead Forecasts* Bulletin, **13**, Nº 3, Center for Ocean-Land-Atmosphere Studies, xx pp [available at http://www.iges.org/ellfb].

Ferreira, D., J. Marshall, and P. Heimbach, 2005: Estimating eddy stresses by fitting dynamics to observations using a residual-mean ocean circulation model and its adjoint. *J. Phys. Oceanogr.*, **35**, 1891–1910.

Fukumori, I., 2002: A partitioned Kalman filter and smoother. *Mon. Weather Rev.*, **130**, 1370–1383.

Fukumori, I., T. Lee, B. Cheng, and D. Menemenlis, 2004: The origins, pathway, and destination of Niño-3 water estimated by a simulated passive tracer and its adjoint. *J. Phys. Oceanogr.*, **34**(3), 582–604.

Gebbie, G., 2004: Subduction in an eddy-resolving state estimate of the Northeast Atlantic Ocean, Ph.D. thesis, Massachusetts Institute of Technology and Woods Hole Oceanographic Institution.

Gent, P. R., and J. C. McWilliams, 1990: Isopycnal mixing in ocean circulation models. *J. Phys. Oceanogr.*, **20**, 150–155.

Goddard L., S. J. Mason, S. E. Zebiak, C. F. Ropelewski, R. Basher and M. A, Cane, 2001: Current approaches to seasonal-to-interannual climate predictions. *Int. J. Climatol.,* **21**, 1111-1152.

Gross, R. S., I. Fukumori, and D. Menemenlis, 2003: Atmospheric and oceanic excitation of the Earth's wobbles during 1980–2000. *J. Geophys. Res.*, **108**(B8), 2370–2386.

Gross, R. S., I. Fukumori, D. Menemenlis, and P. Gegout, 2004: Atmospheric and oceanic excitation of length-of-day variations during 1980–2000. *J. Geophys. Res.*, **109** (B01406).

Harshvardhan, R. D., D. A. Randall and T. G. Corsetti, 1987: A fast radiation parameterization for atmospheric circulation models. *J. Geophys. Res*., **92**, 1009-1016.

Harshvardhan, R. D, D. A. Randall, T. G. Corsetti, and D. A. Dazlich, 1989: Earth radiation budget and cloudiness simulations with a general circulation model. *J. Atmos. Sci.,* **46,** 1922–1942.

Ji M., D. W. Behringer and A. Leetmaa, 1998: An improved coupled model for ENSO prediction and Implications for ocean initialization. Part II: The coupled model. *Mon. Wea. Rev.,* **126**, 1022-1034.

Kim, S.-B., T. Lee, and I. Fukumori, 2004: The 1997-1999 abrupt change of the upper ocean temperature in the north central Pacific. *Geophys. Res. Let.*, **31**, L22304, doi:10.1029/2004GL021,142.

Kirtman B. P. 2003: The COLA anomaly coupled model: ensemble ENSO prediction. . *Mon. Wea. Rev.,* **131**, 2324-2341.

Kistler, R., et al., 2001: The NCEP-NCAR 50-year reanalysis: Monthly means CD-ROM and documentation. *Bull. Amer. Meteor. Soc.*, **82**, 247–268.

Konor C. S., and A. Arakawa, 2005: Incorporation of moist processes and a PBL parameterization into the generalized vertical coordinate model. Technical Report 102, Department of Atmospheric Sciences, UCLA, 63 pp. Available from http://kiwi.atmos.colostate.edu/group/csk

Large, W. G., J. C. McWilliams, and S. Doney, 1994: Oceanic vertical mixing: A review and a model with a nonlocal boundary layer parameterization. *Rev. Geophysics*, **32**, 363–403.

Large, W. G., G. Danabasoglu, S. C. Doney, and J. C. McWilliams, 1997: Sensitivity to surface forcing and boundary layer mixing in a global ocean model: Annual-mean climatology. *J. Phys. Oceanogr.*, **27**, 2418–2447.

Lee, T., and I. Fukumori, 2003: Interannual-to-decadal variations of tropical-subtropical exchange in the Pacific Ocean: Boundary versus interior pycnocline transports. *J. Clim.*, **16**(24), 4022–4042.

Lee, T., I. Fukumori, D. Menemenlis, Z. Xing, and L. Fu, 2002: Effects of the Indonesian Throughflow on the Pacific and Indian oceans. *J. Phys. Oceanogr.*, **32**, 1404–1429.

Marshall, J., A. Adcroft, C. Hill, L. Perelman, and C. Heisey, 1997: A finite-volume, incompressible Navier-Stokes model for studies of the ocean on parallel computers. *J. Geophys. Res.*, **102**(C3), 5753–5766.

Ma, C. -C., C. R. Mechoso, A. W. Robertson, and A. Arakawa, 1996: Peruvian Stratus Clouds and the Tropical Pacific Circulation: A Coupled Ocean-Atmosphere GCM Study, *J. Climate,* **9**, 1635-1645.

McKinley, G. A., M. J. Follows, and J. Marshall, 2003: Interannual variability of air-sea O2 fluxes and the determination of CO2 sinks using atmospheric O2/N2. *Geophys. Res. Let.*, **30**(3), 1101.

Mechoso, C.R., J-Y. Yu and A. Arakawa, 2000: A coupled GCM pilgrimage: from climate catastrophe to ENSO simulations. General Circulation Model Development: Past, Present and Future. Proceedings of a Symposium in Honor of Professor Akio Arakawa, D. A. Randall, Ed., Academic Press, pp. 539-575.

Mechoso, C. R. and co-authors, 1995: The seasonal cycle over the tropical Pacific in general circulation models. *Mon. Weather Rev.*, **123**, 2825-2838.

Menemenlis, D., I. Fukumori, and T. Lee, 2005: Using Green's functions to calibrate an ocean general circulation model. *Mon. Weather Rev.*, **133**, 1224–1240.

Ming J., R. W. Reynolds and D. W. Behringer, 2000: Use of TOPEX/POSEIDON sea level data for analysis and ENSO prediction. Some early results. *J. Climate,* **13**, 216-231.

Paulson, C. A., and J. J. Simpson, 1977: Irradiance measurements in the upper ocean. *J. Phys. Oceanogr.*, **7**, 952–956.

Palmer T. N., A. Alessandri, U. Andersen, P. Cantelaube, M. Davey, P. Délécluse, M. Déqué, E. Díez, F.J. Doblas-Reyes, H. Feddersen, R. Graham, S. Gualdi, J.-F. Guérémy, R. Hagedorn, M. Hoshen, N. Keenlyside, M. Latif, A. Lazar, E. Maisonnave, V. Marletto, A. P. Morse, B. Orfila, P. Rogel, J.-M. Terres, M. C. Thomson,2004: *Bull. Amer. Meteor. Soc.*, **85**, 853–872.

Pan, D. M. and D. A. Randall, 1998: A cumulus parameterization with a prognostic closure. *Quart. J. Roy. Meteor. Soc.,* **124**, 949-981.

Randall D. A. and W. H. Schubert, 2004: Dreams of a stratocumulus sleeper. In Atmospheric Turbulence and Mesoscale Meteorology, Scientific Research Inspires by Doug Lily, E. Federovich, R. Rotuno and B. Stevens (eds.), Cambridge University Press, 95-114.

Redi M. H., 1982: Oceanic isopycnical mixing by coordinate rotation, *J. Phys. Oceanogr.,* **12**, 1154-1158.

Rosati. A., K. Miyakoda and R. Gudgel, 1997: The impact of ocean initial conditions on ENSO forecasting with a coupled model. *Mon. Weather Rev.,* **125**, 754-772.

Saha S., S. Nadiga, C. Thiaw, J. Wang, W. Wang, Q. Zhang, H. M. van den Dool, H.-L. Pan, S. Moorthi, D. Behringer, D. Stokes, M. Peña, S. Lord ,G. White, W. Ebisuzaki, P. Peng, P. Xie, 2006: The NCEP Coupled Forecast System, *J. Climate,* **19**,3483-3517

Segschneider J., D. T. Anderson, J. Vialard, M. Balmaseda, T. N. Stockdale, A. Troccoli and K. Haines, 2001: Initialization of Seasonal forecasts assimilating sea level and temperature observations, *J. Climate,* **14**, 4292-4307.

Stammer, D., C. Wunsch, R. Giering, C. Eckert, P. Heimbach, J. Marotzke, A. Adcroft, C. N. Hill and J. Marshall, 2002: The Global ocean circulation during 1992-1997, estimated from ocean observations and a general circulation model. *J. Geophys.l R.* **107**, (C9), art. 3118. (doi:10.1029/2001JC000888)

Stammer, D., K. Ueyoshi, A. K¨ohl, W. G. Large, S. A. Josey, and C. Wunsch, 2004: Estimating air-sea fluxes of heat, freshwater, and momentum through global ocean data assimilation. *J. Geophys. Res.*, **109**, C05,023.

Troccoli A., and K. Haines, 1999: Use of the temperature salinity relation in a temperature assimilation context. *J. Atmos. Oceanic Technol.*, **16**, 2011-2025.

Wang G., R. Kleeman, N. Smith and F. Tseitkin, 2002: The BRMC coupled general circulation model ENSO forecast system, *Mon. Wea. Rev.,* **130**, 975-991

Wang, O., I. Fukumori, T. Lee, and B. Cheng, 2004a: On the cause of Eastern Equatorial Pacic Ocean T-S variations associated with El Niño. *Geophys. Res. Let.*, **31**, L15309, doi:10.1029/2004GL020,188.

Wang, O., I. Fukumori, T. Lee, and G. Johnson, 2004b: Eastern Equatorial Pacic Ocean T-S variations with El Niño. *Geophys. Res. Let.*, **31**, L04305, doi:10.1029/2003GL019,087.

Wang W., S. Saha, H. L. Pan, S. Nadiga and G. White, 2005: Simulations of ENSO in the new NCEP Coupled Forecast System Model (CFS03), *Mon. Wea. Rev.,* **133**, 1573-1593.

Wilks D. S., 1995: *Statistical Methods in the Atmospheric Sciences.* Academic Press, 464 pp.

Woodruff, S. D., H. F. Diaz, J. D. Elms, and S. J. Worley, 1998: COADS release 2 data and metadata enhancements for improvements of marine surface flux fields. *Phys. Chem. Earth*, **23**, 517–527.

Yu, J. Y. and C. R. Mechoso, 2001: A coupled atmosphere-ocean GCM study of the ENSO cycle. *J. Climate*, **14**, 2329-2350.

Yulaeva, E., M. Kanamitsu, J. Roads, 2007: The ECPC Coupled Prediction Model. *Mon. Wea. Rev.,* in press.

Figures captions

Fig. 1. (a) Mean SST of a 41-year CGCM integration. (b) Mean SST for the 1971–2000 period of the Reynolds SST analysis. Contour interval for (a) and (b) is 2ºC. (c) Difference of (a) minus (b). Contour interval for (c) is 1ºC, zero and negative contour lines are dashed, and negative regions are shaded.

Fig. 2. Hovmöller diagrams for the 41-year simulation averaged between 4ºS to 4ºN. (a) SST anomalies. Contour interval is 1ºC. Contours for +0.5ºC and −0.5ºC are also shown. (b) Zonal wind stress anomalies. Contour interval is 0.1 dyn/cm^2. Contours for +0.05 dyn/cm^2 and −0.05 dyn/cm^2 are also shown.

Fig. 3. Correlation of Niño 3.4 SST index averaged from November to the following February vs. NCEP reanalysis SLP for (a) the 41-year CGCM simulation and (b) NOAA extended SST analysis. Contour interval is 0.1. Only contours above +0.3 or below −0.3 are shown.

Fig. 4. Vertical temperature sections averaged between 2ºS and 2ºN in the Pacific Ocean for the mean 1993–2001 initial conditions for each hindcast set. (a) ECCO initial conditions for March 5. (b) Baseline initial conditions for March 5. (c) ECCO initial conditions for June 5. (d) Baseline initial conditions for June 5. Contour interval is 2ºC.

Fig. 5. Difference between the mean initial conditions shown in Fig. 4 and the corresponding March or June CGCM climatology. (a) ECCO minus CGCM on March 5. (b) Baseline minus CGCM on March 5. (c) ECCO minus CGCM on June 5. (d) Baseline minus CGCM on June 5. Contour interval is 1 ºC.

Fig. 6. Differences between mean DJF SST hindcasts and CGCM climatology. (a) ECCO DJF hindcasts initialized on March 5 minus CGCM DJF climatology. (b) Baseline March hindcasts minus CGCM. (c) ECCO June hindcasts minus CGCM. (d) Baseline June hindcasts minus CGCM. Contour interval is 1 ºC.

Fig. 7. Skill of DJF SST anomaly forecasts for (a) ECCO forecasts initialized on March-5, (b) baseline forecasts initialized on March-5, (c) persistence forecasts initialized in March, (d) ECCO forecasts initialized on June-5, (e) baseline forecasts initialized on June-5, and (f) persistence forecasts initialized in June. Contour interval is 0.1. Only contours above 0.6 or below −0.6, which are significant at the 95% confidence level, are shown.

Fig. 8. Standard error of forecasted DJF SST anomalies for the same six cases as in Fig. 7. Contour interval is 0.5ºC.

Fig. 9. (a) Difference of Fig. 8b minus Fig. 8a. (b) Difference of Fig. 8e minus Fig. 8d. Shaded areas exceed 95% statistical significance (see text for details). Contour interval is 0.25ºC.

Fig. 10. Skill as a function of time lead for the ECCO, the baseline, and the persistence hindcasts of Niño 3.4 SST monthly anomalies for (a) hindcasts initialized in March and (b) hindcasts initialized in June.

Fig. 11. Standard error as a function of time lead for the ECCO, the baseline, and the persistence hindcasts of Niño 3.4 SST monthly anomalies for (a) hindcasts initialized in March and (b) hindcasts initialized in June.

Fig. 12. Intra-ensemble standard deviation (forecast spread) of DJF SST for each hindcast set. (a) ECCO March hindcasts. (b) Baseline March hindcasts. (c) ECCO June hindcasts. (d) Baseline June hindcasts. Contour interval is 0.25ºC.

Fig. 13. Equatorial Pacific vertical sections of standard deviation for interannual temperature anomalies averaged between 2ºS and 2ºN during the 1993−2001 period. (a) ECCO March 5 initial solutions. (b) Baseline March 5 initial conditions. (c) Difference: (a) minus (b). Contour interval is 0.5ºC.

Fig. 14. Baseline minus ECCO difference of the 1993–2001 standard deviation of Pacific Ocean temperature anomaly hindcasts from March-5 initial conditions, averaged between 2ºS and 2ºN, for (a) the March–May period, (b) the June–August period, (c) the September–November period, and (d) the December–February period. Contour interval is 0.5ºC.

Fig. 15. Time evolution of skill and standard error for Niño 3.4 SST anomalies hindcasts, for ECCO, NCEP's CFS and ECMWF hindcasts. (a) Skill for ECCO March-5, CFS from March and ECMWF from February and from May hindcasts, (b) Standard error (ºC) for the hindcasts of (a), (c) skill for ECCO June-5, CFS from June and ECMWF from May and August hindcasts, (d) standard error for the hindcasts of (c). Period considered is 1993–2001 in all the cases.

Fig. 16. Correlation of December–February Niño 3.4 SST index to Pacific Ocean temperature averaged between 2ºS and 2ºN for (a) the March-5 ECCO initial conditions, (b) the March-5 baseline initial conditions, (c) the June-5 ECCO initial conditions, and (d) the June-5 baseline initial conditions. Contour interval is 0.1. Only values above 0.6 or below −0.6 are shown.

Table 1: Brier skill scores for hindcasts of the Niño-3.4 index above its median during the DJF period, with respect to a climatological forecast of probability 0.5. Values with statistical significance above the 95% level are highlighted in boldface.

ECCO March	*Baseline March*	*ECCO June*	*Baseline June*
0.38	0.11	**0.57**	**0.52**

Table 2. Comparison of results from this study (UCLA/MIT CGCM) with state-of-the-art CGCM seasonal ENSO forecast systems for 6-months-lead hindcasts of the Niño-3.4 SST anomaly index. ECHAM/MOM and COLA/MOM CGCMs are described by De Witt et al. (2004a,b); ECMWF CGCM is described by Palmer et al. (2004); and NCEP CFS is described by Saha et al. (2006). All comparisons are carried out for the 1993–2001 period except for the ECHAM/MOM and COLA/MOM estimates, for which the 1993–2001 statistics could not be derived from publicly available results.

GCMC	***Initial conditions***	***Period of hindcasts***	***Started from***	***Skill measure, 6 months lead***	***Standard error, 6 months lead***
UCLA/MIT	ECCO	1993–2001	March	0.80	0.62ºC
			June	0.94	0.55ºC
	Baseline	1993-2001	March	0.80	1.2ºC
			June	0.95	0.80ºC
ECHAM/MOM	In house	1982-2003	April	0.6	0.9ºC
			July	0.8	0.9ºC
COLA/MOM	In house	1982-2003	April	0.6	1.0ºC
			July	0.8	1.1ºC
ECMWF	ECMWF	1993-2001	Feb.	0.63	0.62ºC
			May	0.91	0.49ºC
			Aug.	0.95	0.39ºC
NCEP CFS	GODAS	1993-2001	March	0.77	0.7ºC
			June	0.90	0.55ºC

Table 3. Comparison of skill and standard errors of DJF Niño 3.4 SST anomaly index for the hindcasts sets of this study considering the whole 1993-2001 data set and excluding 1997-1998 episode.

	Skill for DJF N34 index, whole 1993-2001 sets	***Skill for DJF N34 index, excluding 1997-1998 episode***	***Standard error for DJF N34 index, whole 1993-2001 sets***	***Standard error for DJF N34 index, whole 1993-2001 sets***
ECCO from March	0.85	0.73	0.71ºC	0.71ºC
Baseline from March	0.85	0.71	1.20ºC	1.16ºC
ECCO from June	0.95	0.88	0.41ºC	0.44ºC
Baseline from June	0.95	0.88	0.68ºC	0.69ºC

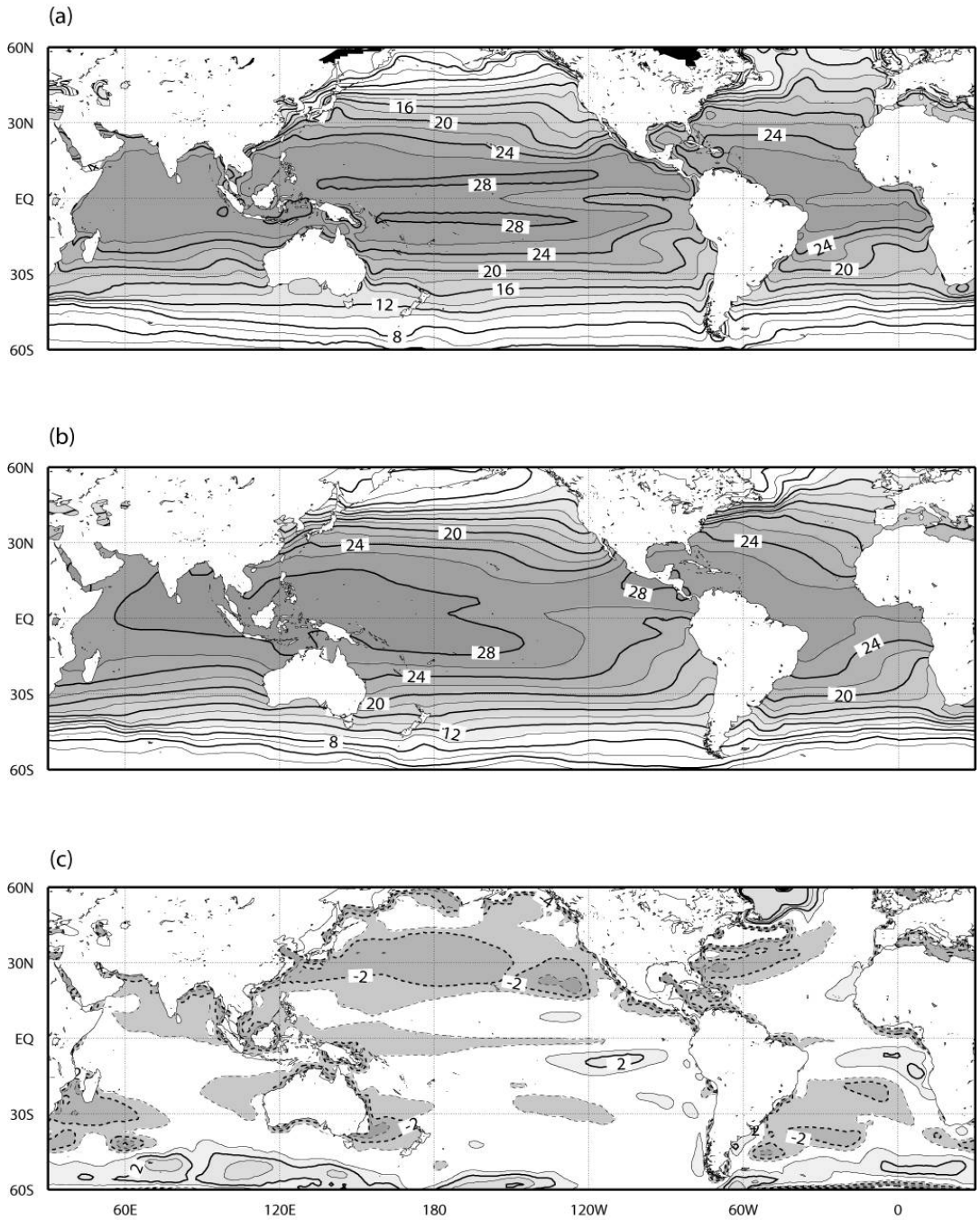

Fig. 1. (a) Mean SST of a 41-year CGCM integration. (b) Mean SST for the 1971–2000 period of the Reynolds SST analysis. Contour interval for (a) and (b) is 2ºC. (c) Difference of (a) minus (b). Contour interval for (c) is 1ºC, zero and negative contour lines are dashed, and negative regions are shaded.

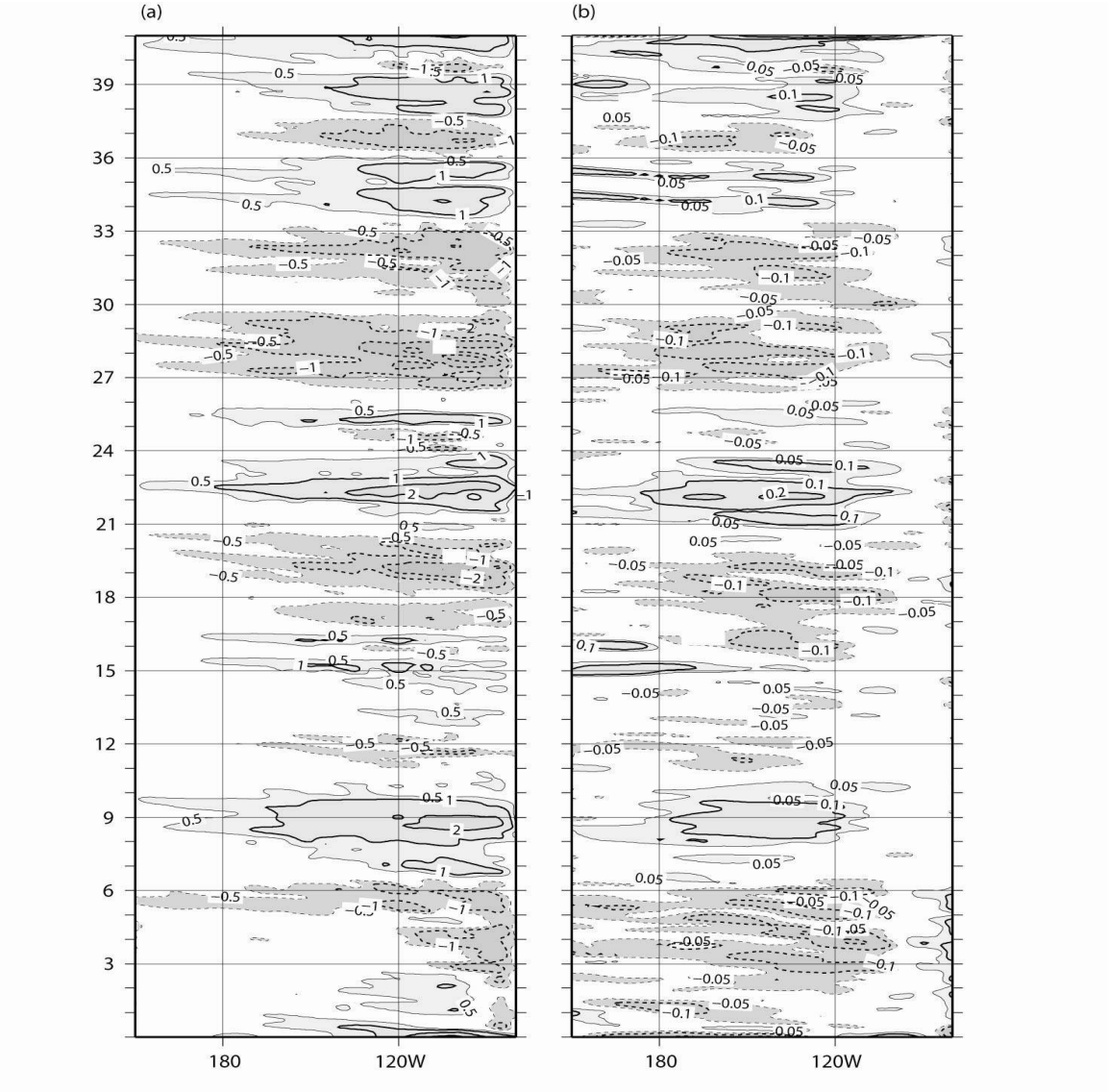

Fig. 2. Hovmöller diagrams for the 41-year simulation averaged between 4ºS to 4ºN. (a) SST anomalies. Contour interval is 1ºC. Contours for +0.5ºC and −0.5ºC are also shown. (b) Zonal wind stress anomalies. Contour interval is 0.1 dyn/cm^2. Contours for +0.05 dyn/cm^2 and −0.05 dyn/cm^2 are also shown.

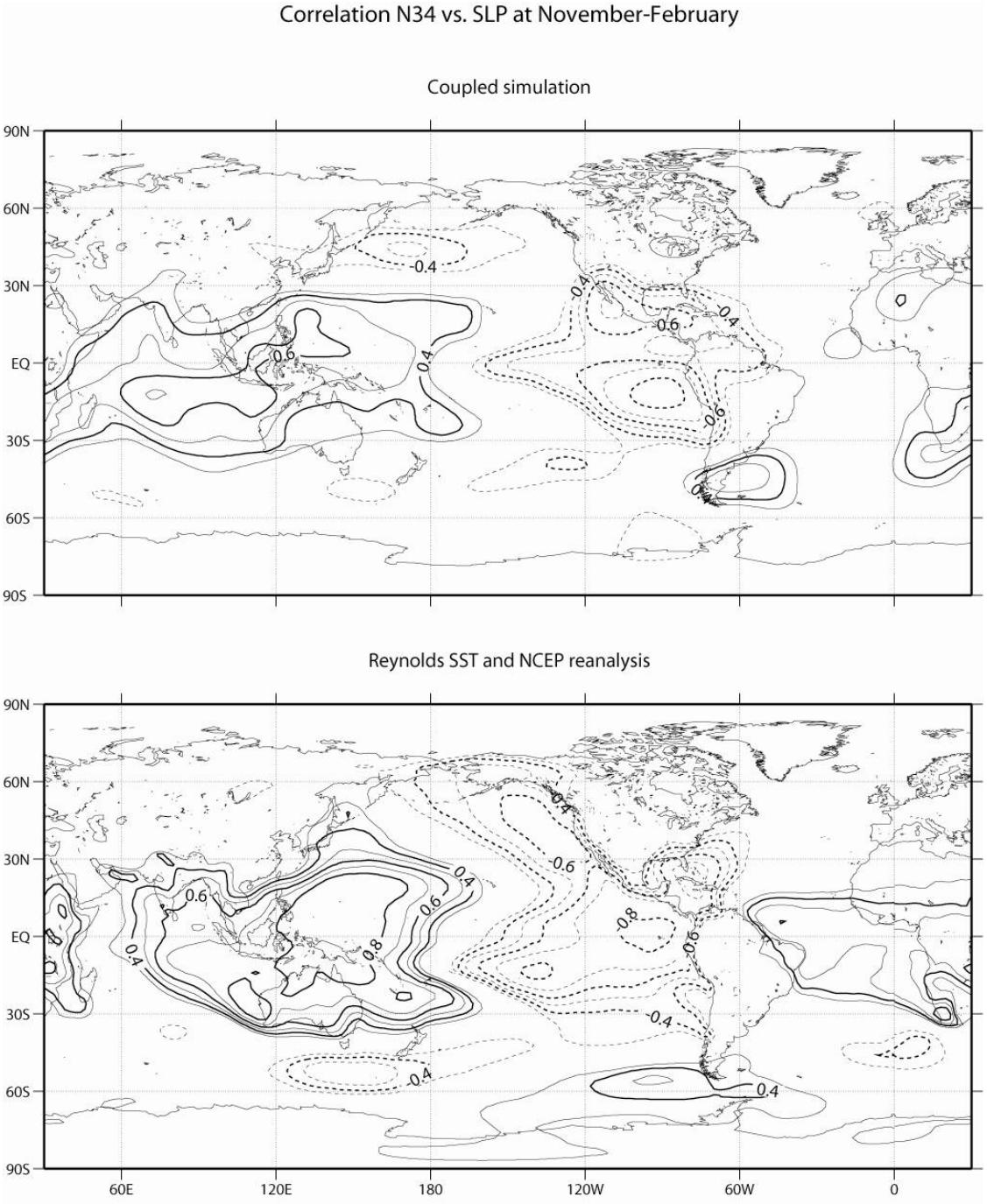

Fig. 3. Correlation of Niño 3.4 SST index averaged from November to the following February vs. NCEP reanalysis SLP for (a) the 41-year CGCM simulation and (b) NOAA extended SST analysis. Contour interval is 0.1. Only contours above +0.3 or below −0.3 are shown.

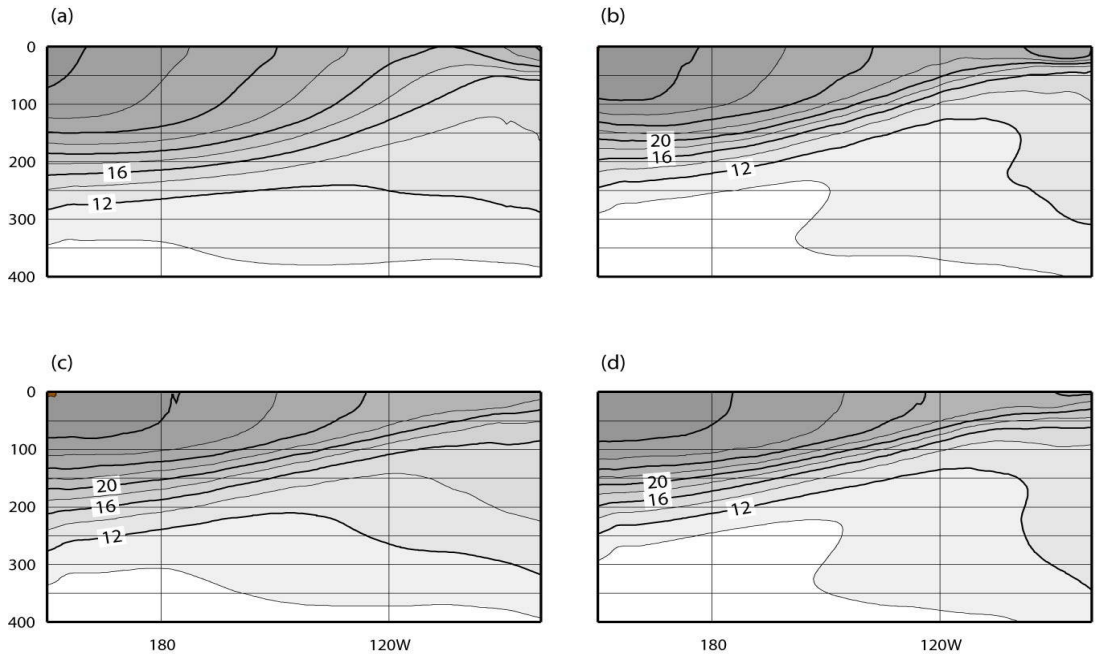

Fig. 4. Vertical temperature sections averaged between 2ºS and 2ºN in the Pacific Ocean for the mean 1993–2001 initial conditions for each hindcast set. (a) ECCO initial conditions for March 5. (b) Baseline initial conditions for March 5. (c) ECCO initial conditions for June 5. (d) Baseline initial conditions for June 5. Contour interval is 2ºC.

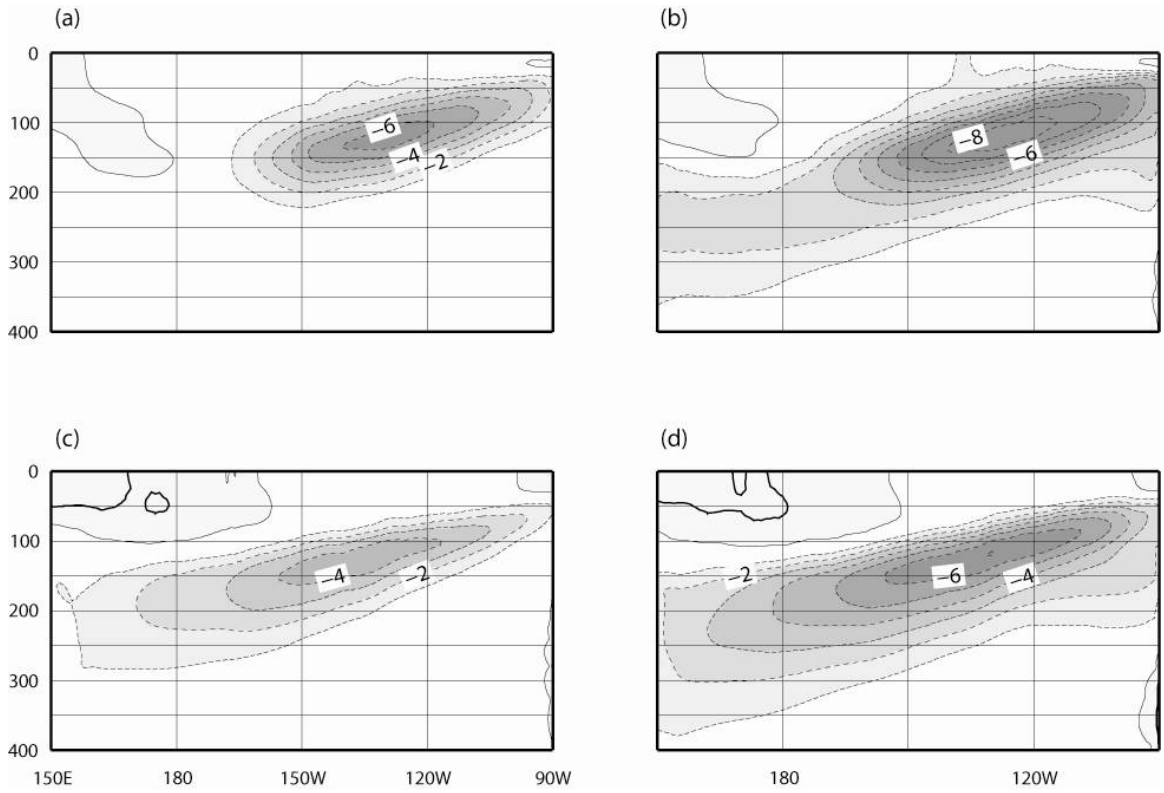

Fig. 5. Difference between the mean initial conditions shown in Fig. 4 and the corresponding March or June CGCM climatology. (a) ECCO minus CGCM on March 5. (b) Baseline minus CGCM on March 5. (c) ECCO minus CGCM on June 5. (d) Baseline minus CGCM on June 5. Contour interval is 1 ºC.

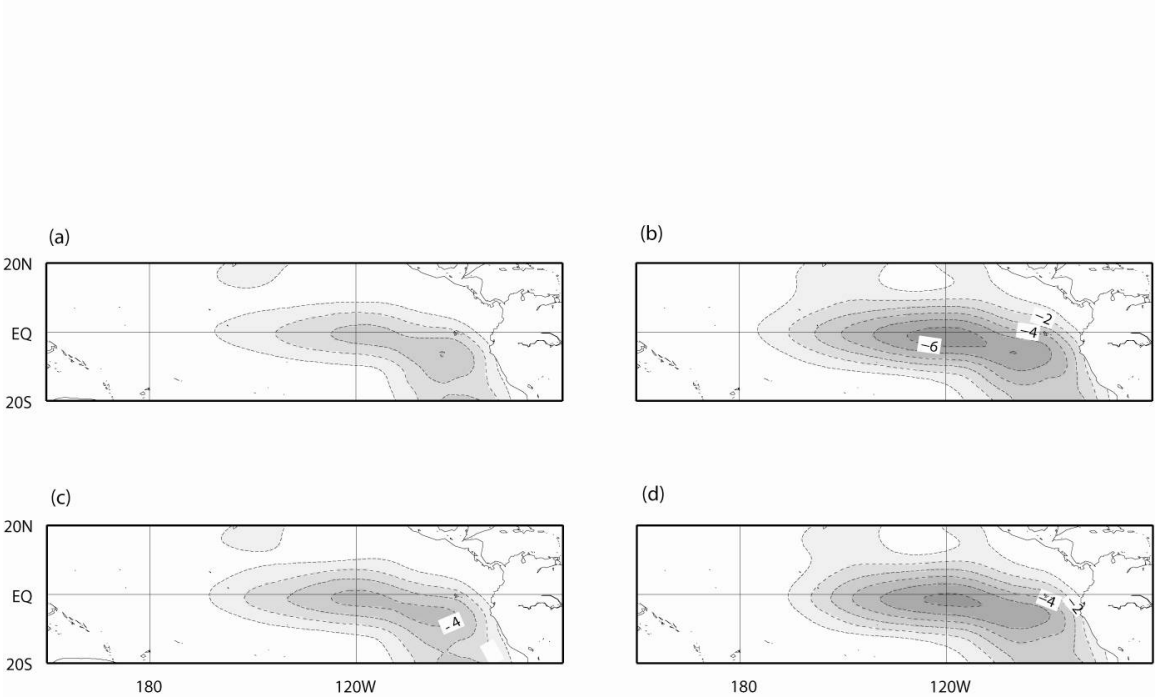

Fig. 6. Differences between mean DJF SST hindcasts and CGCM climatology. (a) ECCO DJF hindcasts initialized on March 5 minus CGCM DJF climatology. (b) Baseline March hindcasts minus CGCM. (c) ECCO June hindcasts minus CGCM. (d) Baseline June hindcasts minus CGCM. Contour interval is 1 ºC.

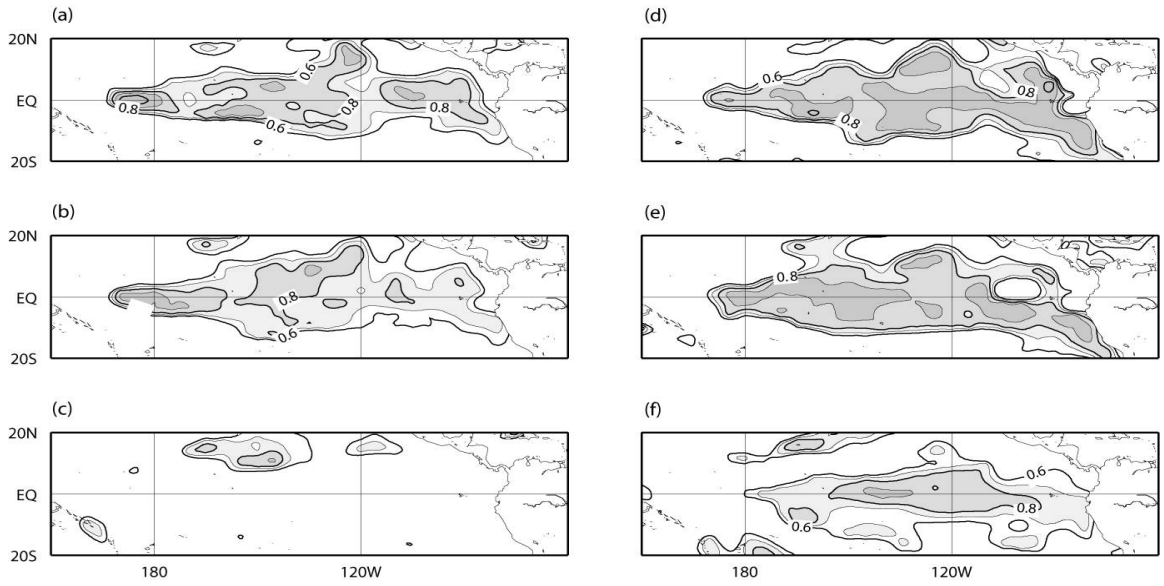

Fig. 7. Skill of DJF SST anomaly forecasts for (a) ECCO forecasts initialized on March-5, (b) baseline forecasts initialized on March-5, (c) persistence forecasts initialized in March, (d) ECCO forecasts initialized on June-5, (e) baseline forecasts initialized on June-5, and (f) persistence forecasts initialized in June. Contour interval is 0.1. Only contours above 0.6 or below −0.6, which are significant at the 95% confidence level, are shown.

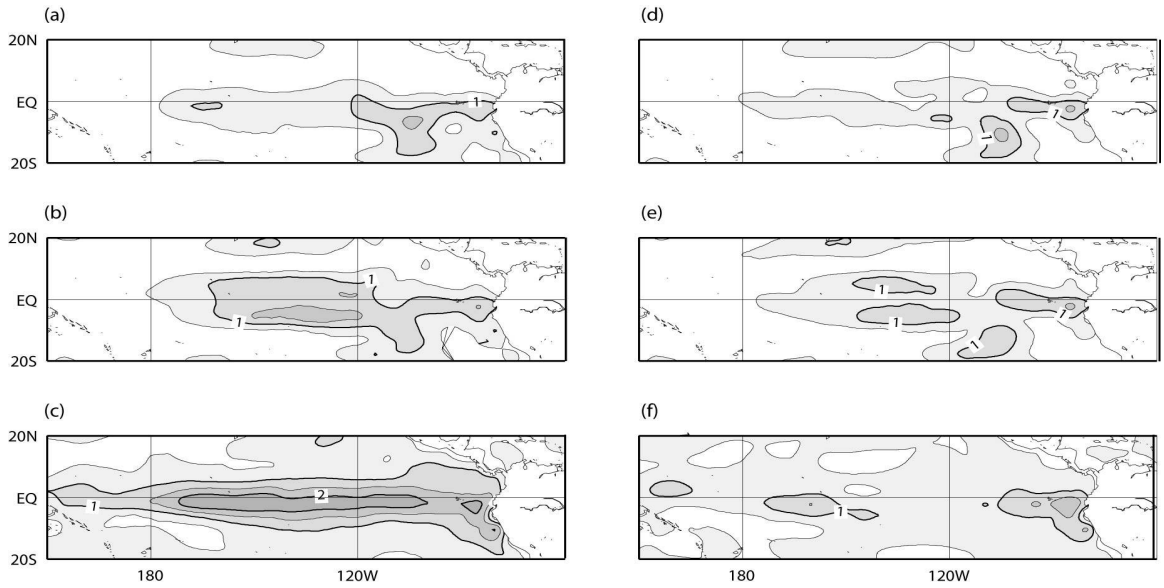

Fig. 8. Standard error of forecasted DJF SST anomalies for the same six cases as in Fig. 7. Contour interval is 0.5ºC.

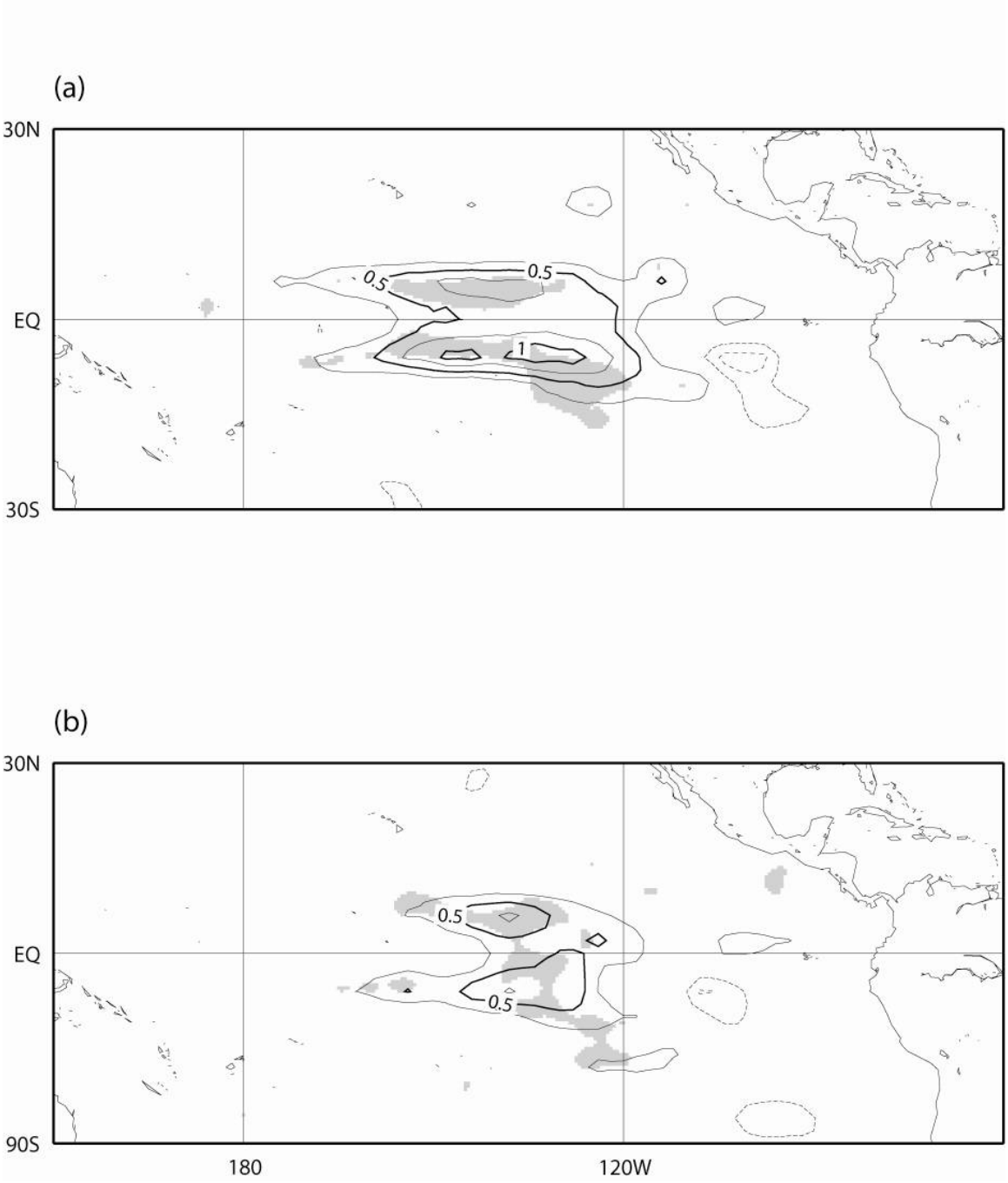

Fig. 9. (a) Difference of Fig. 8b minus Fig. 8a. (b) Difference of Fig. 8e minus Fig. 8d. Shaded areas exceed 95% statistical significance (see text for details). Contour interval is 0.25ºC.

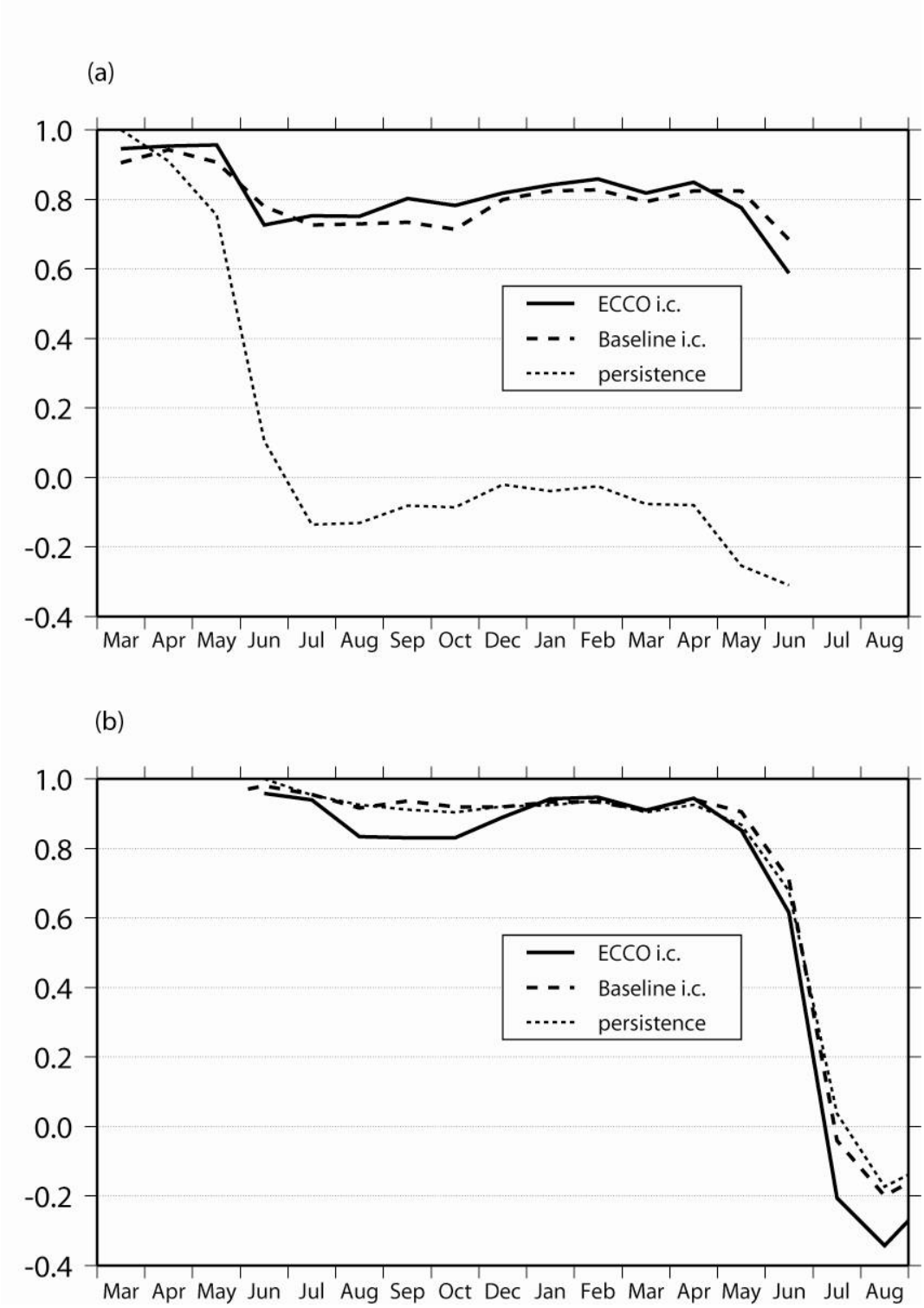

Fig. 10. Skill as a function of time lead for the ECCO, the baseline, and the persistence hindcasts of Niño 3.4 SST monthly anomalies for (a) hindcasts initialized in March and (b) hindcasts initialized in June.

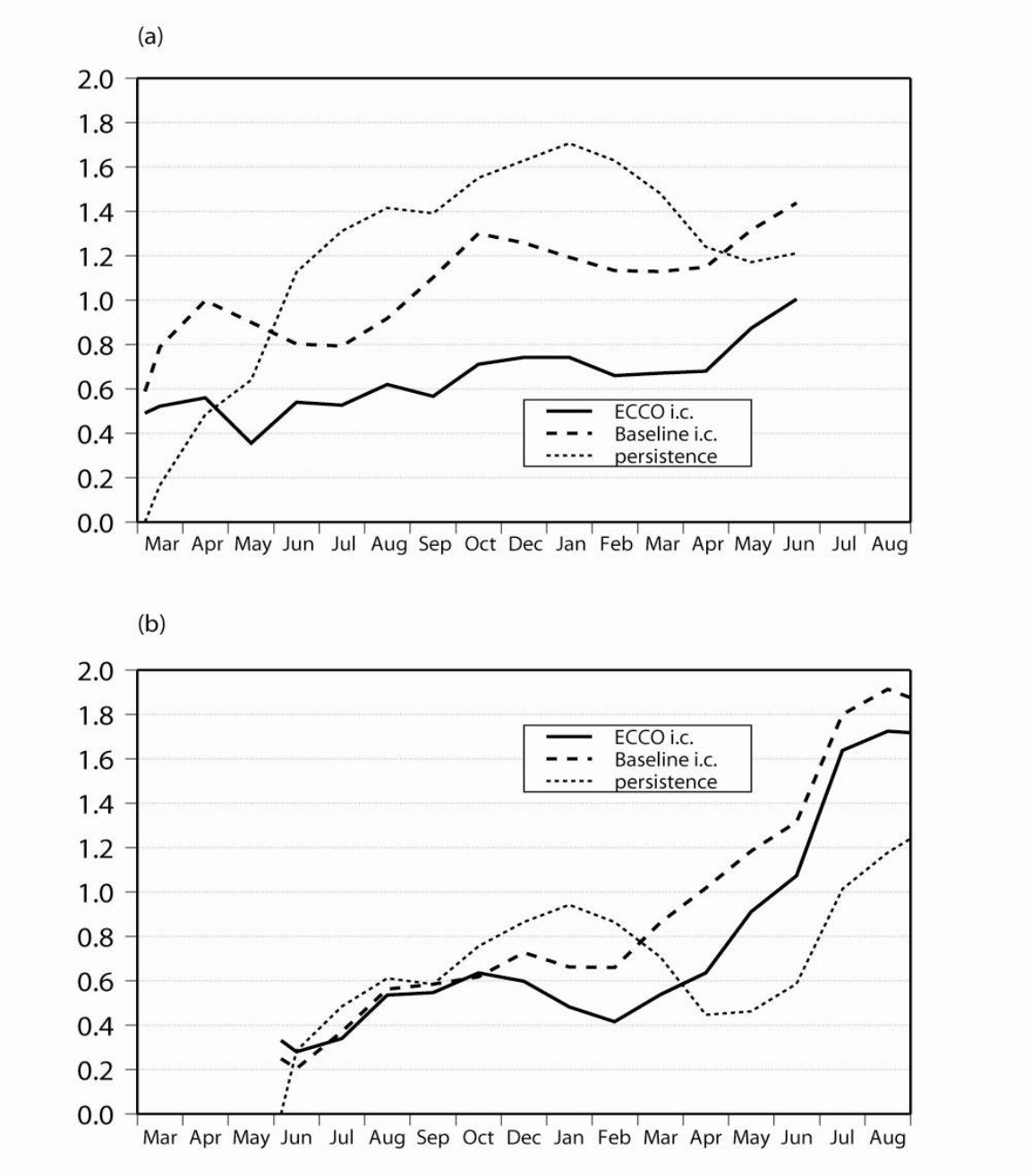

Fig. 11. Standard error as a function of time lead for the ECCO, the baseline, and the persistence hindcasts of Niño 3.4 SST monthly anomalies for (a) hindcasts initialized in March and (b) hindcasts initialized in June.

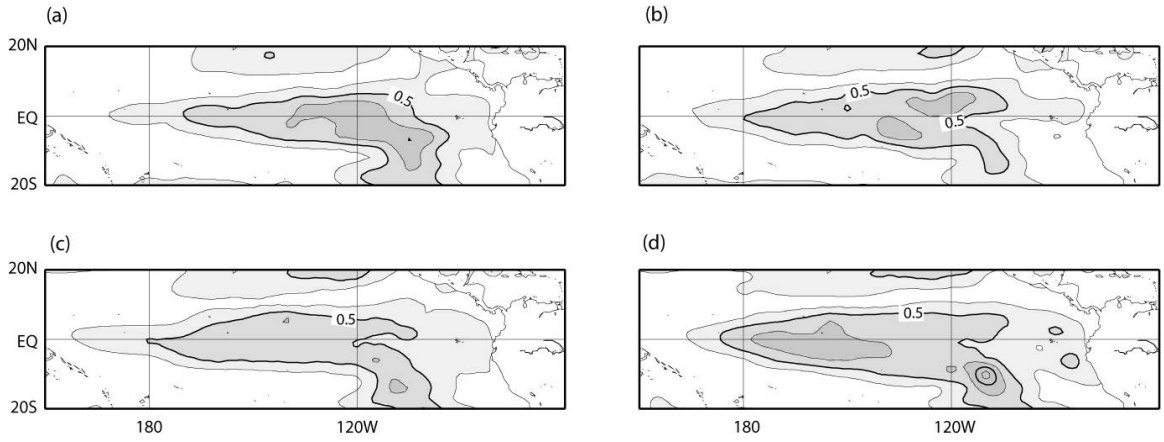

Fig. 12. Intra-ensemble standard deviation (forecast spread) of DJF SST for each hindcast set. (a) ECCO March hindcasts. (b) Baseline March hindcasts. (c) ECCO June hindcasts. (d) Baseline June hindcasts. Contour interval is 0.25ºC.

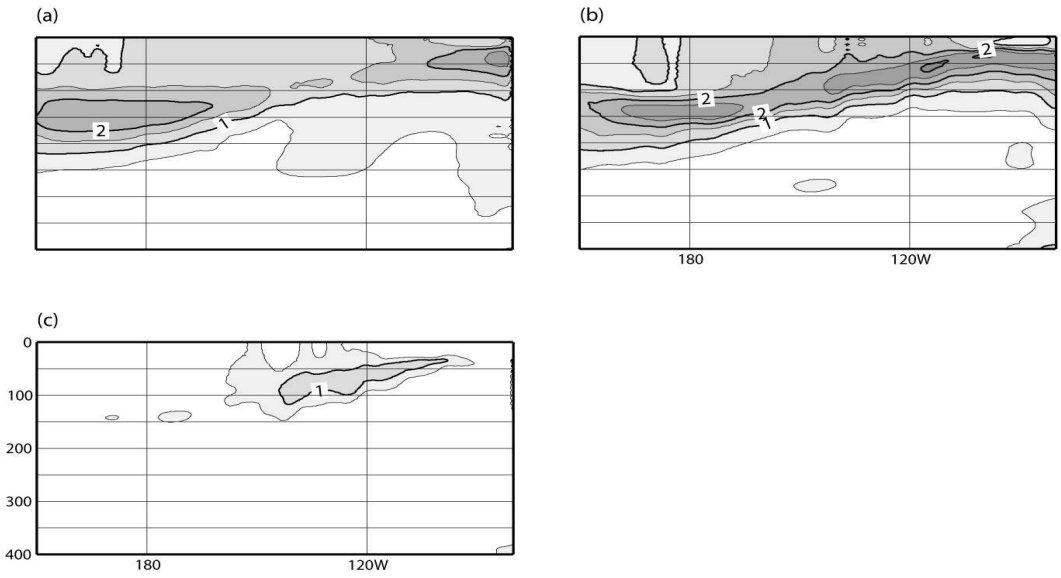

Fig. 13. Equatorial Pacific vertical sections of standard deviation for interannual temperature anomalies averaged between 2ºS and 2ºN during the 1993−2001 period. (a) ECCO March 5 initial solutions. (b) Baseline March 5 initial conditions. (c) Difference: (a) minus (b). Contour interval is 0.5ºC.

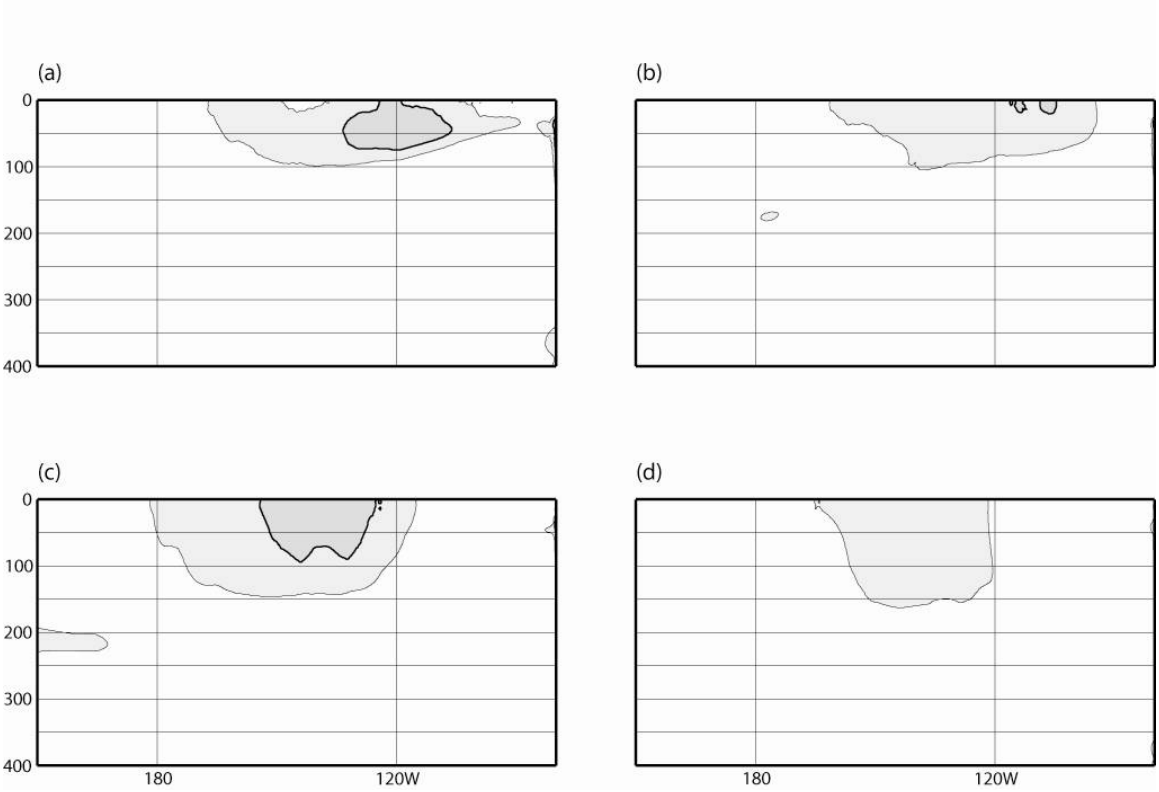

Fig. 14. Baseline minus ECCO difference of the 1993–2001 standard deviation of Pacific Ocean temperature anomaly hindcasts from March-5 initial conditions, averaged between 2ºS and 2ºN, for (a) the March–May period, (b) the June–August period, (c) the September–November period, and (d) the December–February period. Contour interval is 0.5ºC.

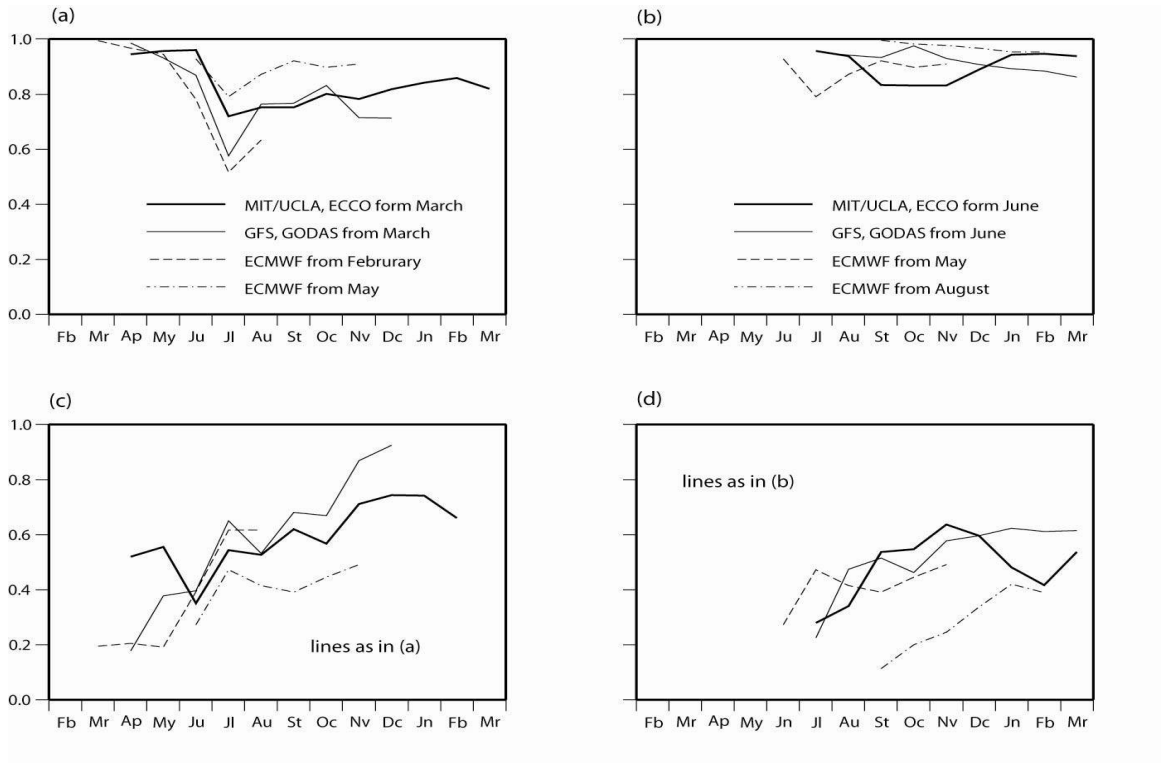

Fig. 15. Time evolution of skill and standard error for Niño 3.4 SST anomalies hindcasts, for ECCO, NCEP's CFS and ECMWF hindcasts. (a) Skill for ECCO March-5, CFS from March and ECMWF from February and from May hindcasts, (b) Standard error (ºC) for the hindcasts of (a), (c) skill for ECCO June-5, CFS from June and ECMWF from May and August hindcasts, (d) standard error for the hindcasts of (c). Period considered is 1993–2001 in all the cases.

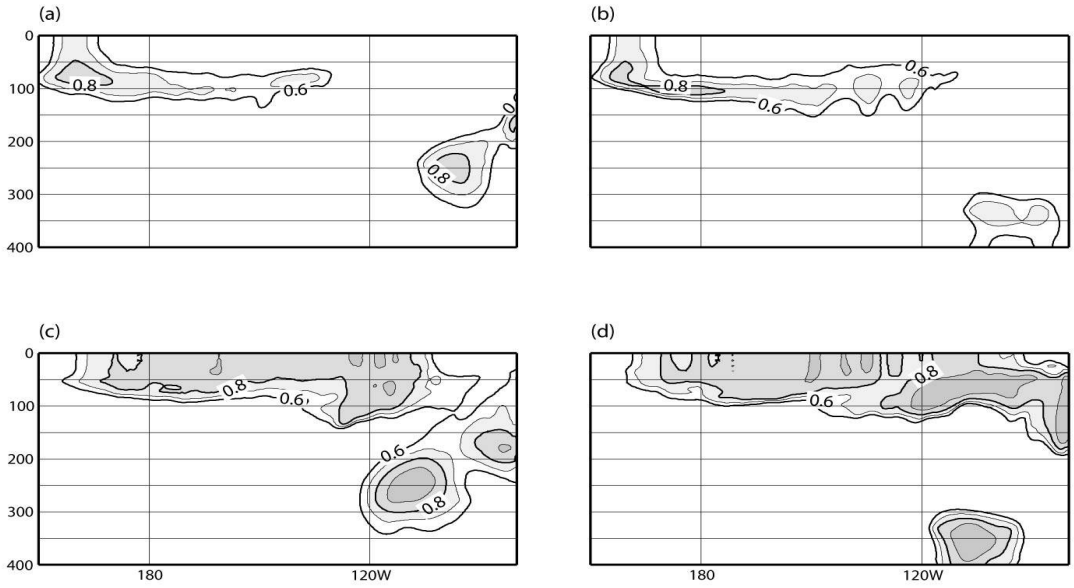

Fig. 16. Correlation of December–February Niño 3.4 SST index to Pacific Ocean temperature averaged between 2ºS and 2ºN for (a) the March-5 ECCO initial conditions, (b) the March-5 baseline initial conditions, (c) the June-5 ECCO initial conditions, and (d) the June-5 baseline initial conditions. Contour interval is 0.1. Only values above 0.6 or below −0.6 are shown.